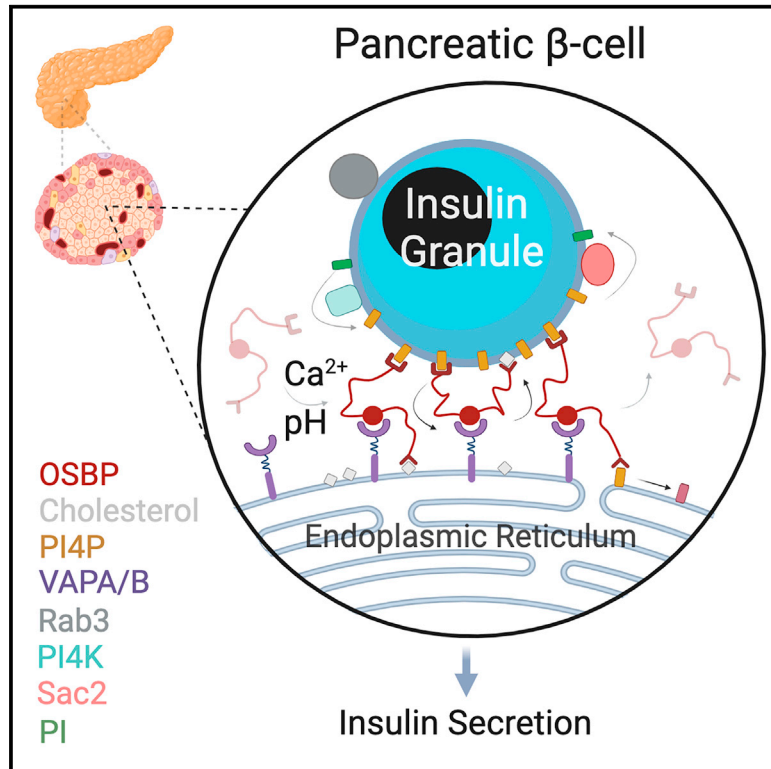


OSBP-mediated PI(4)P-cholesterol exchange at endoplasmic reticulum-secretory granule contact sites controls insulin secretion

Graphical abstract



Authors

Styliani Panagiotou, Kia Wee Tan, Phuoc My Nguyen, ..., Anders Tengholm, Michele Solimena, Olof Idevall-Hagren

Correspondence

olof.idevall@mcb.uu.se

In brief

Panagiotou et al. find that the ER forms membrane contact sites with insulin-containing secretory granules. OSBP is recruited to these sites in a Ca^{2+} and pH-dependent mechanism and catalyzes the exchange of granule PI(4)P for ER cholesterol. This OSBP-mediated lipid exchange is required for normal insulin secretion.

Highlights

- The ER forms physical contacts with insulin-containing secretory granules (SGs)
- Oxysterol-binding protein (OSBP) catalyzes PI(4)P/cholesterol exchange at ER-SG contacts
- OSBP is spatio-temporally regulated by changes in the intracellular Ca^{2+} concentration and pH
- PI(4)P/cholesterol exchange at ER-SG contacts is required for normal insulin secretion



Article

OSBP-mediated PI(4)P-cholesterol exchange at endoplasmic reticulum-secretory granule contact sites controls insulin secretion

Styliani Panagiotou,¹ Kia Wee Tan,^{1,8} Phuoc My Nguyen,^{1,8} Andreas Müller,^{2,3,4} Affiong Ika Oqua,⁵ Alejandra Tomas,⁵ Anna Wendt,^{6,7} Lena Eliasson,^{6,7} Anders Tengholm,¹ Michele Solimena,^{3,4,5} and Olof Idevall-Hagren^{1,9,*}

¹Department of Medical Cell Biology, Uppsala University, Uppsala, Sweden

²Molecular Diabetology, University Hospital and Faculty of Medicine Carl Gustav Carus, TU Dresden, Dresden, Germany

³Paul Langerhans Institute Dresden (PLID) of the Helmholtz Center Munich at the University Hospital Carl Gustav Carus and Faculty of Medicine of the TU Dresden, Dresden, Germany

⁴German Center for Diabetes Research (DZD e.V.), Neuherberg, Germany

⁵Section of Cell Biology and Functional Genomics, Division of Diabetes, Endocrinology and Metabolism, Department of Metabolism, Digestion and Reproduction, Imperial College London, London, UK

⁶Department of Clinical Sciences, Lund University, Lund, Sweden

⁷Lund University Diabetes Center (LUDC), Lund, Sweden

⁸These authors contributed equally

⁹Lead contact

*Correspondence: olof.idevall@mcb.uu.se

<https://doi.org/10.1016/j.celrep.2024.113992>

SUMMARY

Insulin is packaged into secretory granules that depart the Golgi and undergo a maturation process that involves changes in the protein and lipid composition of the granules. Here, we show that insulin secretory granules form physical contacts with the endoplasmic reticulum and that the lipid exchange protein oxysterol-binding protein (OSBP) is recruited to these sites in a Ca^{2+} -dependent manner. OSBP binding to insulin granules is positively regulated by phosphatidylinositol-4 (PI4)-kinases and negatively regulated by the PI4 phosphate (PI(4)P) phosphatase Sac2. Loss of Sac2 results in excess accumulation of cholesterol on insulin granules that is normalized when OSBP expression is reduced, and both acute inhibition and small interfering RNA (siRNA)-mediated knockdown of OSBP suppress glucose-stimulated insulin secretion without affecting insulin production or intracellular Ca^{2+} signaling. In conclusion, we show that lipid exchange at endoplasmic reticulum (ER)-granule contact sites is involved in the exocytic process and propose that these contacts act as reaction centers with multimodal functions during insulin granule maturation.

INTRODUCTION

Blood glucose homeostasis critically depends on the appropriate release of insulin from pancreatic β cells. Insulin is produced as a pro-peptide that is packaged into secretory granules (SGs) that bud from the trans-Golgi network. These immature granules undergo a series of maturation steps that involve changes in the composition of both granular lipids and proteins and that coincide with the maturation of insulin.¹ A typical β cell contains between 5,000 and 15,000 SGs,^{2,3} but only around 50–100 of these have the ability to fuse with the plasma membrane.^{4,5} These granules belong to the readily releasable pool and are situated at the plasma membrane where they await a triggering Ca^{2+} signal. Prolonged stimulation of insulin secretion will deplete this pool and new SGs must be recruited from the large reserve pool to sustain secretion. This recruitment primarily involves newly synthesized SGs and depends on granule transport along microtubules as well as acquisition of specific priming and docking factors and interactions with components of the secretory machinery, including t-

SNARE family members and voltage-dependent Ca^{2+} channels.^{4,6–10} Defects in the replenishment of release-competent SGs have been observed in type-2 diabetes and likely contribute to disease development.¹¹

The mechanisms by which SGs dock and fuse with the plasma membrane are well characterized and to a large extent similar to those of other neuro-endocrine cells. However, the steps preceding the arrival of granules at the plasma membrane are largely unclear. These steps include the action of numerous small GTPases, including Rab3, Rab27, and Rab2, and the corresponding Rab effectors, but it is not well understood how these reactions are regulated.¹ Progression through the endo-lysosomal system requires the cooperative action of Rabs and phosphoinositides, which together control the recruitment of both phosphoinositide-metabolizing enzymes and Rab effectors and ensures unidirectionality throughout the membrane trafficking cascade.¹² To what extent the same principal guides progression through the regulated secretory pathway is not known. The trans-Golgi network is rich in phosphatidylinositol 4-phosphate (PI(4)P), and this lipid is



directly involved in the formation of nascent SGs via recruitment of the GTPase Arf1.^{13,14} The membrane of the newly formed SGs likely contains high concentrations of PI(4)P, both as a consequence of its Golgi origin and through the action of PI4-kinases.¹⁵ We recently described the involvement of the PI(4)P phosphatase Sac2 in insulin SG maturation and exocytosis.¹⁶ Lack of Sac2 resulted in accumulation of PI(4)P on the SG surface and in an inability of granules to stably dock and fuse with the plasma membrane. This mechanism resembles vesicle maturation in yeast cells, where the endoplasmic reticulum (ER)-localized PI(4)P phosphatase Sac1 is recruited to the vesicle surface.¹⁷ In these cells, recruitment occurs through an interaction with the lipid transport protein Osh4p, which also directly contributes to PI(4)P removal by exchanging it for cholesterol.^{17,18} To what extent a similar mechanism operates during regulated secretion is not known. However, observations that loss of the mammalian Osh4p homolog OSBP leads to impaired insulin secretion and that SG cholesterol accumulation is required for insulin release are consistent with the existence of such a mechanism.^{19–21}

Here, we now show that loss of Sac2 in β cells results in excess accumulation of cholesterol on the surface of insulin SGs through an OSBP-dependent process. Recruitment of OSBP to the granule surface is controlled by granular PI(4)P and dynamically regulated by cytosolic Ca^{2+} and pH, with knockdown or inhibition of OSBP resulting in impaired insulin secretion. These results unravel an SG maturation pathway in β cells and also demonstrate a role of ER-SG contact sites in regulated secretion.

RESULTS

ER-SG contact sites

Ultrastructural examination of β cells from mouse pancreatic islets of Langerhans using transmission electron microscopy revealed the presence of ribosome-free ER domains in close proximity to insulin SGs (Figure 1A). To obtain a more detailed view of these contacts, we performed volumetric reconstruction of individual ER-granule contacts in focused ion beam (FIB) scanning electron microscopy data of mouse β cells.²² We frequently observed ribosome-free ER in close proximity (10–20 nm) to insulin-containing SGs, and in many cases the ER traced the outlines of the granules in a pattern resembling membrane contact sites (MCSs) (Figures 1B and 1C).^{23–25} Next, we performed proximity ligation assays (PLAs) in fixed mouse islets using antibodies against the general ER marker Sec61 β and the granule marker Rab3. We detected, on average, five fluorescent puncta per imaging plane and β cell, indicating positions where the ER and SG are within 40 nm of each other (Figures 1D, 1E, 1G, and S1). Next, we repeated the PLA using antibodies against VAP-A, an ER protein commonly involved in MCS formation, and Rab3. This resulted in a 4-fold increase in the number of detected PLA puncta (Figures 1F and 1G), despite very similar distribution patterns of Sec61 β and VAP-A in traditional immunofluorescence staining (Figure S1). This indicates that VAP-A may be enriched at the ER-SG interface. We also detected some PLA signals from islet cells negative for insulin, suggesting that close proximities between ER and SG also exist in other islet cell types (Figures 1E and 1F).

Next, we wanted to determine whether these contacts existed in live cells and to explore their putative dynamics. We therefore

developed a proximity sensor based on dimerization-dependent fluorescent proteins.²⁶ This sensor makes use of two quenched monomers, RA and GB, that form a fluorescent heterodimer when brought in proximity to each other. To test the applicability of this method for visualization of MCSs, we designed a version for reporting ER-PM contact sites by targeting RA to the surface of the ER using Sec61 β and GB to the plasma membrane through C-terminal lipidation (GB-CaaX). Co-expression of these two constructs resulted in a distinct fluorescence pattern that was restricted to the cell periphery and overlapped with an ER marker (Figure S2A). As a positive control, we targeted both RA and GB to the ER, resulting in strong fluorescence (Figure S2B), and as a negative control we expressed either GB-CaaX or RA-Sec61 β alone (Figures S2C and S2D).²⁶ To determine within what range of distances from each other the two moieties must be to form a fluorescent protein, we fused GB to the N or C terminus of ER-localized Extended-Synaptotagmin 3 (E-Syt3) and expressed it together with RA-CaaX. Although C-terminally localized GB was able to boost RA fluorescence at the plasma membrane, we could not detect any fluorescence signal from cells expressing N-terminally localized GB, indicating that a gap distance <20 nm is required (Figure S2E).²⁷

To visualize ER-SG contacts using this system, we needed a suitable SG marker accessible from the cytosol. We chose Rab3, which according to the PLA experiments (see Figure 1), was present on ER-adjacent SGs and also is a well-established marker of mature, release-competent SGs.²⁸ We performed a pulse-chase experiment in MIN6 cells co-expressing GFP-Rab3 and NPY-Halo (a luminal SG protein) (Figure 2A). First, all Halo molecules were labeled by the addition of the ligand JFX650. After 1 h, the same cells were exposed to the spectrally separable ligand JFX549, and the cells were then chased for 2 h. Consistent with Rab3 labeling mature granule, we observed pronounced co-localization of Rab3 and NPY-Halo^{JFX650} at time point 0, while NPY-Halo^{JFX549} was largely absent from the Rab3-positive SGs. After 2 h, the proportion of SG positive for NPY-Halo^{JFX549} and Rab3 increased significantly and was similar to that of NPY-Halo^{JFX650} at time point 0 (Figures 2B and 2C). These results show that Rab3 localize to granules that departed the Golgi within the last 1–2 h, reflecting the time required for SG maturation.²⁹ Having confirmed that Rab3 labels mature granules, we next localized GB to the surface of SGs by fusing it to Rab3 and co-expressed it with RA-Sec61 β . This resulted in strong punctate fluorescence that overlapped with markers of both the ER (ER-oxGFP) (Figures 2D–2F) and SGs (NPY-mNG) (Figures 2G and 2H). All puncta overlapped with both the ER marker and SG marker, but not all SG were positive for the contact site reporter (Figures 2G and 2H). This demonstrates the existence of a sub-population of SGs defined by physical tethering to the ER. Time-lapse imaging revealed that the contacts were dynamic and moved together with SGs, indicating physical tethering, and not just proximity, to the ER (Figures 2I and 2J).

OSBP localizes to ER-SG contact sites in a PI(4)P-dependent manner

MCSs are hubs for lipid-exchange reactions. Oxysterol-binding protein 1 (OSBP) is a lipid-exchange protein that localizes to MCSs by binding to VAPs in the ER membrane and PI(4)P in the

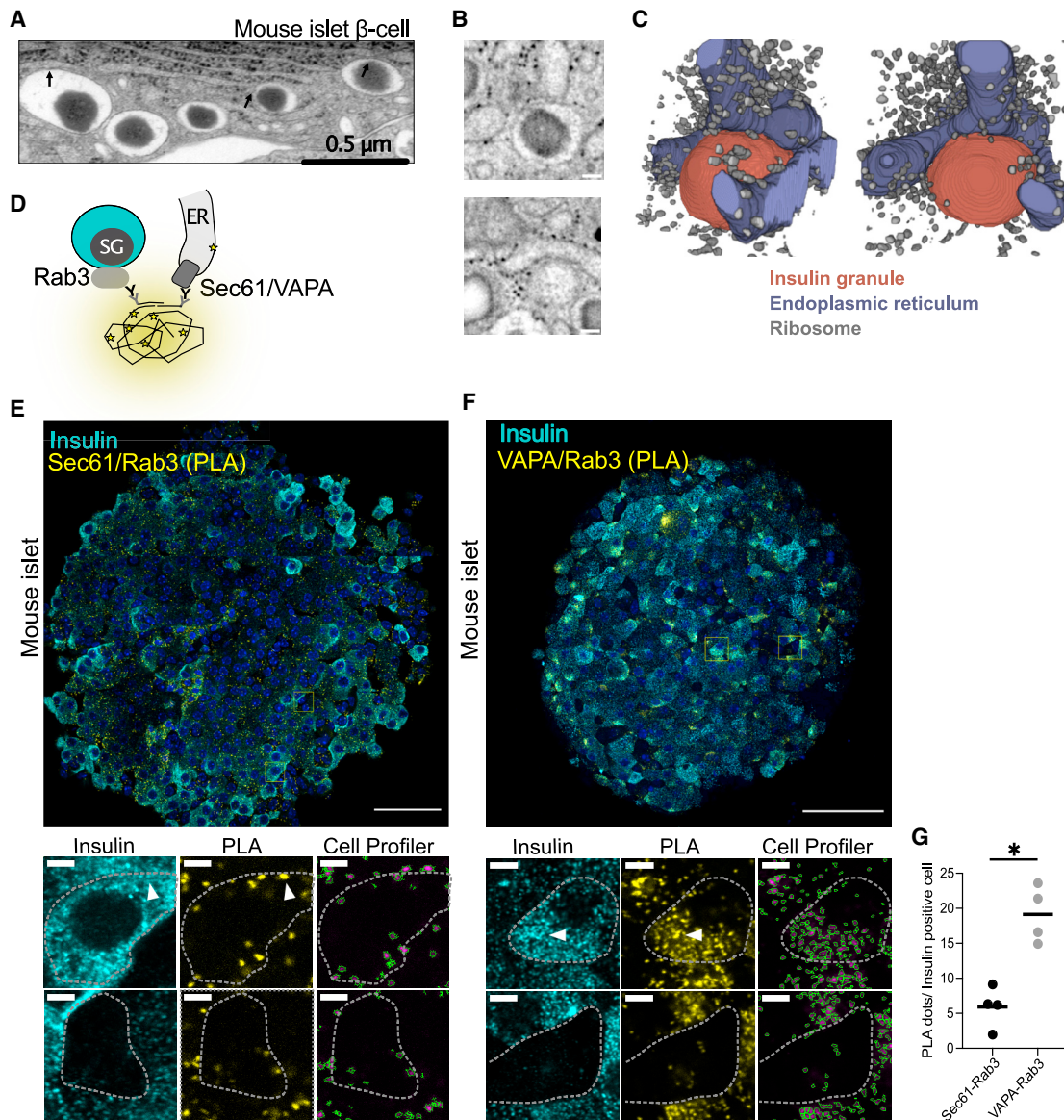


Figure 1. MCSs between the ER and insulin secretory granules

(A) Transmission electron microscopy image of a mouse islet β cell showing close proximities between insulin granules and the ER (arrows). (B) x-y slices at different z positions from FIB-scanning electron microscopy images showing the proximity between an insulin granule and the ER in a mouse β cell. Scale bar: 100 nm. (C) Volumetric renderings of (B) showing the insulin granule in red, the ER in blue, and ribosomes in gray. (D) Principle of PLA for detection of ER-insulin granule contacts using antibodies against the ER (Sec61 β /VAP-A) and insulin granules (Rab3a). (E and F) Confocal microscopy images of mouse islets with insulin immunostaining shown in cyan and ER-granule contact sites detected with PLA and shown in yellow. Scale bar: 50 μ m. PLA with Sec61 β /Rab3 is shown in (E) and PLA with VAP-A/Rab3 in (F). Magnified images below show insulin-containing β cells (top pair) and non- β cells (bottom pair) containing contact sites, and segmentation/detection of contact sites with Cell Profiler. Scale bar: 5 μ m. Arrows in magnified images identify PLA puncta overlapping with insulin granules. Scale bars: 50 μ m/5 μ m (magnified). (G) Average number of PLA puncta per insulin-positive cell (single confocal plane) detected using the indicated antibody pairs. (n = 4 islets for each antibody pair, p < 0.05, unpaired, two-tailed Student's t test).

target membrane.^{24,30,31} It is primarily found at the ER-Golgi interface where it exchanges Golgi PI(4)P for ER cholesterol.^{24,32} Immunofluorescence imaging of MIN6 β cells and mouse islets showed that OSBP primarily localized to a peri-nuclear compartment that stained positive for the Golgi marker GolgB1

(Figures 3A, 3B, and 3D). Preincubation with the OSBP inhibitor OSW-1 (20 nM, 30 min), which blocks lipid exchange and stabilizes OSBP at PI(4)P-rich membranes, caused a striking redistribution of OSBP from the Golgi to insulin SGs (Figures 3A–3E). Next, we visualized this redistribution by confocal microscopy

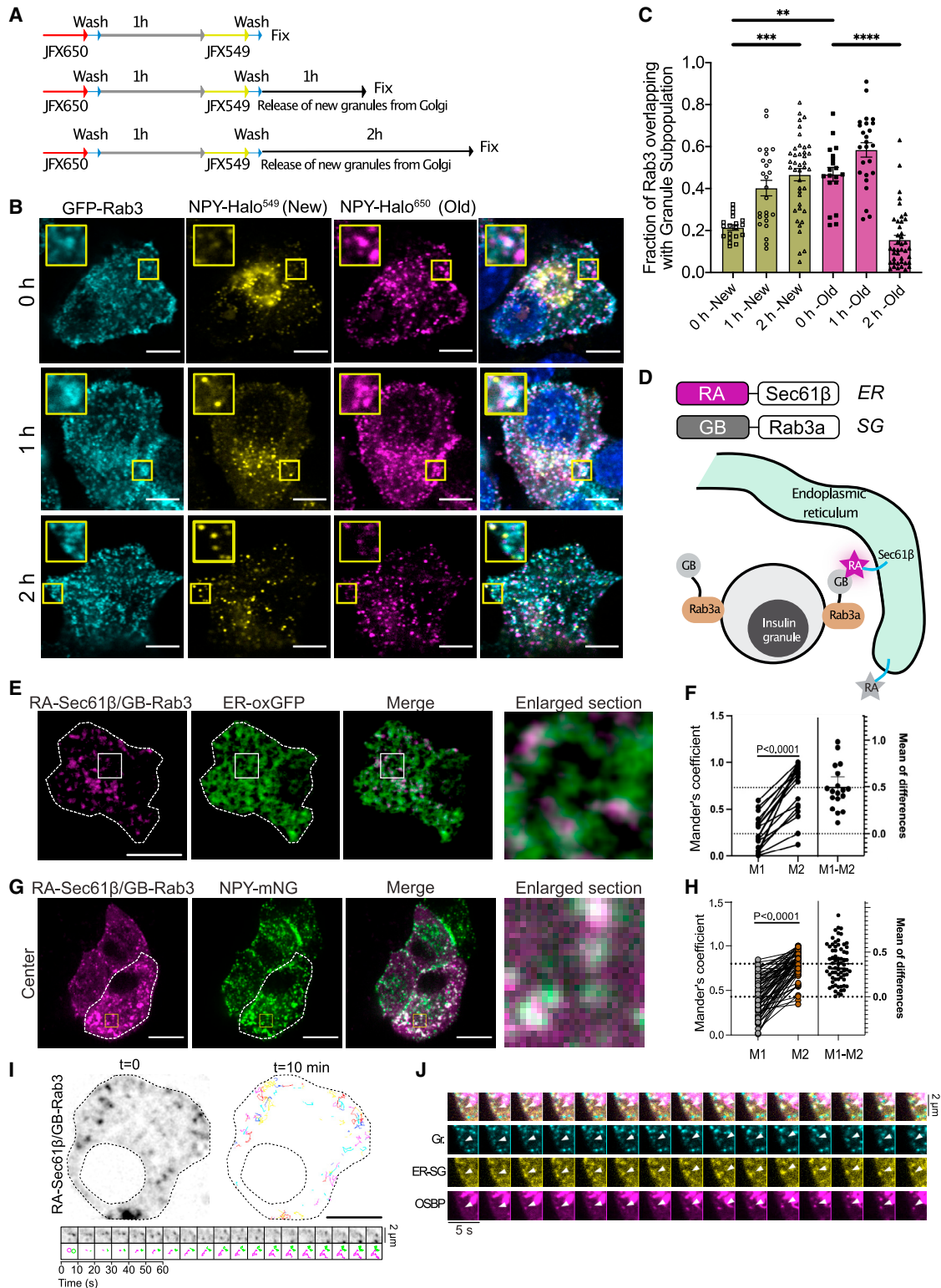


Figure 2. Dimerization-dependent fluorophore reporter for ER-SG contact sites

(A) Schematic of pulse-chase experiment. MIN6 cells expressing GFP-Rab3 and NPY-Halo were first labeled with JFX650 Halotag ligand for 20 min (red) to visualize all existing granules and block Halotag reactive sites. The dye was then washed out and new NPY-Halo was synthesized by cells for 1 h (gray), which was

(legend continued on next page)

in live MIN6 cells expressing fluorescently tagged OSBP (Halo^{JFX646}-OSBP) and the SG marker NPY-mNG. Halo^{JFX646}-OSBP had a predominant Golgi localization and was only found on 2%–5% of the SG (Figures 4A and 4B). Strikingly, addition of OSW-1 resulted in rapid enrichment of Halo^{JFX646}-OSBP on SGs, with 10%–20% of the SGs being positive for OSBP after 30-min incubation with OSW-1 (Figures 4A and 4B). To test whether these were the same SG that were in contact with the ER, we again took advantage of the dimerization-dependent fluorescent protein. We made a version where OSBP was fused to the non-fluorescent GB-subunit (GB-OSBP) and co-expressed this together with RA-Sec61 β and the SG marker NPY-mNeonGreen (NPY-mNG). Under resting conditions, there was essentially no red fluorescence overlapping with NPY-mNG, indicating the absence of OSBP at ER-SG contacts. Addition of 20 nM OSW-1 resulted in the rapid appearance of red fluorescent puncta that overlapped with, or were in close proximity to, NPY-mNG, demonstrating that OSBP becomes enriched at ER-SG contacts (Figures 4C and 4D). Since OSBP stabilization at MCSs typically requires binding to the ER-localized VAPs, we next tested how OSBP recruitment to SG was affected by siRNA-mediated knockdown of VAP-A and VAP-B in rat insulinoma INS-1 832/3 cells. In control cells, 30-min incubation with OSW-1 induced the expected accumulation of OSBP at SGs, but this response was completely absent in cells with reduced VAP expression (Figure 4G). Immunofluorescence staining of VAP-A or VAP-B and insulin revealed proximity between the both VAPs and SG, but, in contrast to OSBP, there was no further enrichment of either VAP at SGs following incubation with OSW-1 (Figures S3A–S3D). Importantly, the addition of OSW-1 was also without effect on the overall Golgi and ER morphology (Figures S3E–S3G). Next, we tested whether the OSW-1-induced recruitment of OSBP to SGs contributed to ER-SG contact site formation. We expressed the ER-SG proximity reporter together with the SG marker NPY-mNG and visualized them by confocal microscopy before and following addition of 20 nM OSW-1. In contrast to its effect on OSBP, OSW-1 was without effect on the number of ER-SG contacts, suggesting that OSBP is recruited to pre-existing MCSs (Figures 4E and 4F).

OSBP interacts with PI(4)P in target membranes through its C-terminal PH domain.³⁰ To test whether PI(4)P binding was required for OSBP recruitment to SGs, we expressed the Halo-tagged wild-type or PI(4)P-binding-deficient (RR107/108EE) PH domain of OSBP and treated the cells with OSW-1, followed by immunostaining against insulin and visualization by confocal microscopy. We found that the wild-type PH domain was effectively recruited onto 10% of insulin SGs, while the PI(4)P-binding-deficient version was not, indicating a role of SG PI(4)P in OSBP recruitment (Figures 5A and 5B). PI(4)P is primarily produced from phosphatidylinositol through the action of PI4-kinases. To test whether the binding of OSBP to SG depended on local PI4-kinase activity, we pre-treated cells expressing Halo^{JFX646}-OSBP and NPY-mNG with PI4-kinase inhibitors and exposed them to OSW-1. We found that the recruitment of Halo^{JFX646}-OSBP to SG was prevented by the broad PI4-kinase inhibitor phenylarsineoxide (PAO) but not by the more selective class III β (PIK93 and PI4KI) or class III α (GSK-A1) inhibitors (Figures 5C, 5D, and S4). Immunostainings as well as live-cell imaging revealed the presence of class II α PI4-kinases on insulin SGs, making this a likely candidate for maintaining the granular PI(4)P pool (Figures 4E–4G).

OSBP binding to SGs is regulated by Ca²⁺ and cytosolic pH

The distinct SG localization of OSBP following addition of OSW-1 indicates the existence of constitutive weak or transient interactions between OSBP and SGs that are stabilized by preventing PI(4)P extraction. We next asked whether such stabilization could be accomplished under more physiological conditions. The binding of OSBP to the Golgi is counteracted by increases in the cytosolic Ca²⁺ concentration, likely through inhibition of PI4-kinases with accompanying reduction in Golgi PI(4)P.^{33,34} Ca²⁺ is a key second messenger in β cells, and glucose stimulation causes voltage-dependent Ca²⁺ influx that triggers insulin SG exocytosis. To test whether voltage-dependent Ca²⁺ influx had an impact on OSBP distribution, we depolarized MIN6 β cells expressing GFP-OSBP or Halo^{JFX646}-OSBP while observing the cells by confocal microscopy. We found that Ca²⁺ influx triggered the immediate dissociation of OSBP from the Golgi (Figures 6A, 6B, and S5) but

then selectively labeled with the JFX549 Halotag ligand (yellow). After the specified chase time, the cells were fixed, processed, and imaged to determine the kinetics of Rab3 acquisition onto insulin granules.

(B) Confocal images of fixed MIN6 cells expressing GFP-Rab3 (amplified with GFP-booster Alexa Fluor 488) in cyan, newly synthesized and packaged NPY-Halo^{JFX549} (yellow), and previously existing NPY-Halo^{JFX650} (magenta). Chase times indicated on the left after 549 labeling. Scale bar: 5 μ m.

(C) Mander's coefficients denoting the fraction of Rab3 overlapping new (549-labeled) and old (JFX650-labeled) insulin granules. Rab3 progressively marks newly synthesized insulin granules as they mature (n = 21–32 cells from three experiments; Kruskal-Wallis followed by Dunn's *post hoc* test; **p < 0.01, ***p < 0.005, ****p < 0.001).

(D) Diagram showing the use of conditional fluorophores as a probe for ER-granule contacts. The ER-targeted dimerization-dependent RFP (RA) dimerizes with the granule targeted non-fluorescent booster (GB), revealing ER-SG contact sites.

(E) Confocal microscopy images of a MIN6 cell expressing the ER-marker ER-oxGFP (green) and the RA-Sec61 β /GB-Rab3 contact site reporter (magenta). Scale bar: 5 μ m.

(F) Quantification of the colocalization between ER and the contact site reporter (M1) and the contact site reporter and ER (M2) (n = 17 cells; two-tailed Student's t test).

(G) Confocal microscopy images of MIN6 cells expressing the insulin granule marker NPY-mNG (green) and the RA-Sec61 β /GB-Rab3 contact site reporter (magenta). Scale bar: 10 μ m.

(H) Quantification of the colocalization between granules and the contact site reporter (M1) and the contact site reporter and granules (M2) (n = 53 cells; two-tailed Student's t test).

(I) Confocal microscopy image of a MIN6 cell expressing the ER-SG contact site reporter (left) and an image showing the trajectories for selected contacts during 10 min of continuous imaging (right). Bottom panel shows a time series for two of the ER-SG contacts. Images have been inverted for clarity. Scale bar: 5 μ m.

(J) Time series from a MIN6 cell expressing the granule marker NPY-mNG (Gr., cyan), the ER-SG contact site reporter (yellow), and Halo^{JFX650}-OSBP (magenta).

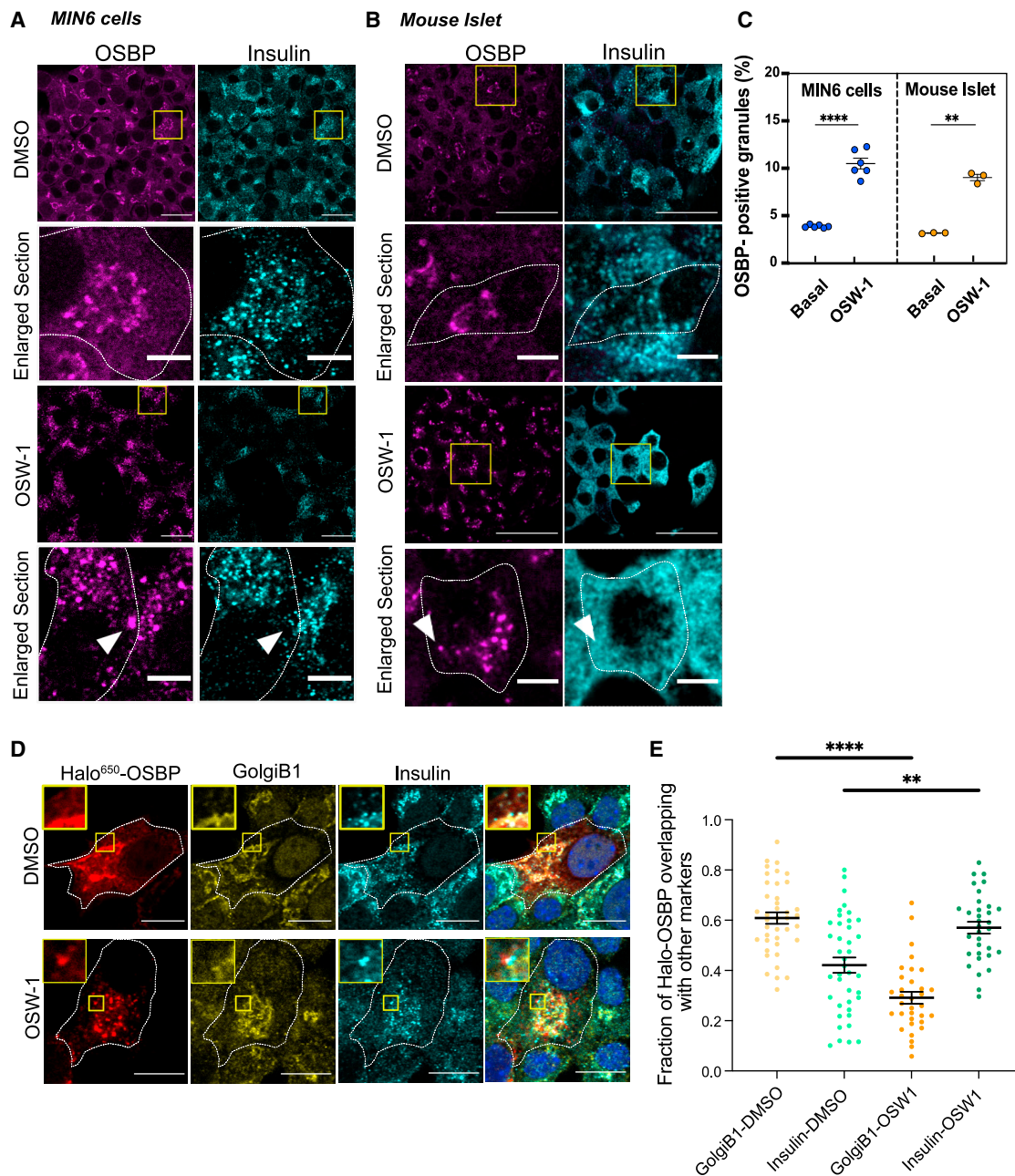


Figure 3. OSBP is recruited to insulin granules after OSW-1 treatment in fixed cells

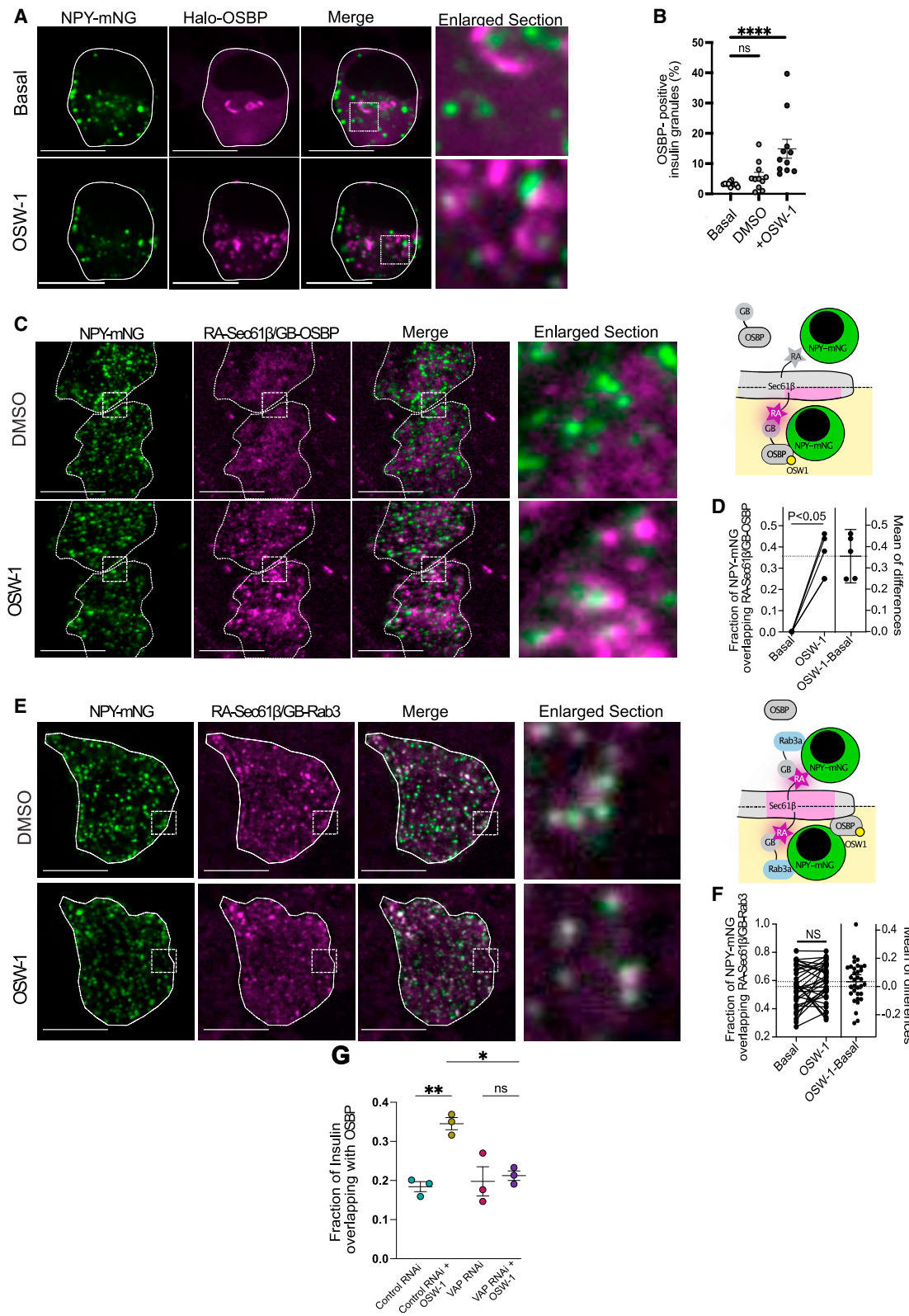
(A) Confocal microscopy images of MIN6 cells treated with OSW-1 (20 nM for 20 min) or vehicle (DMSO) and immunostained for insulin (cyan) and OSBP (magenta). Enlarged sections are magnified from boxed regions. Arrowheads show an overlapping punctum. Scale bars: 20 and 5 μ m.

(B) Confocal microscopy images of a mouse islet treated with OSW-1 (20 nM for 20 min) or vehicle (DMSO) and immunostained for insulin (cyan) and OSBP (magenta). Enlarged sections are magnified from boxed regions. Scale bars: 20 and 5 μ m.

(C) Quantification of fraction of OSBP-positive insulin granules in MIN6 cells and mouse islet β cells treated with OSW-1 (20 nM for 20 min) or DMSO (basal). Each dot represents the mean of one experiment and line shows mean for all experiments (** $p < 0.01$, **** $p < 0.0001$; $n = 6$ and 3 experiments with >50 cells or >10 islets per experiment, two-tailed, unpaired Student's t test).

(D) Confocal microscopy images of MIN6 cells expressing Halo^{JFX650}-OSBP (red), treated with OSW-1 (20 nM for 20 min) or DMSO, and fixed and immunostained against GolgiB1 (yellow) and insulin (cyan). Insets are magnifications of the boxed areas. Scale bar: 5 μ m.

(E) Fraction of Halo-OSBP fluorescence overlapping with the Golgi and insulin granule compartments in cells treated with OSW-1 or vehicle. Means \pm SEM with dots representing single cells (** $p < 0.01$, **** $p < 0.0001$; $n = 32$ –38 cells, two-tailed, unpaired Student's t test).



(legend on next page)

did not prevent OSBP binding to the ER (Figures 6C–6F). Similar displacement of OSBP was also seen in response to Ca^{2+} release from the ER triggered by the addition of carbachol (Figure S5E) and in response to an elevation of the glucose concentration from 3 to 20 mM (Figures 6L–6N). These experiments show that Ca^{2+} elevations trigger the release of OSBP from the Golgi, perhaps making it available for interactions at other MCSs. PI(4)P was recently shown to act as a pH sensor through protonation at acidic pH, which results in reduced affinity for effector proteins.³⁵ Depolarization of β cells is associated with acidification of the cytosol,³⁶ and we therefore tested whether pH changes may contribute to OSBP displacement. To accomplish rapid pH changes, we exposed MIN6 cells to 10 mM NH_4Cl . This caused a rapid alkalization, seen as an increase in BCECF fluorescence. Washout of NH_4Cl resulted in transient acidification that was followed by pH normalization within 1 min (Figure S5C). Subsequently, we exposed MIN6 cells expressing GFP-OSBP and loaded with the Ca^{2+} indicator Cal590 to 10 mM NH_4Cl . The acute alkalization was without effect on cytosolic Ca^{2+} or OSBP localization, while washout of NH_4Cl caused dramatic dissociation of GFP-OSBP from the Golgi without accompanying change in cytosolic Ca^{2+} (Figures 6G–6I). Importantly, alkalization of the cytosol with 10 mM NH_4Cl completely prevented the depolarization-induced dissociation of GFP-OSBP from the Golgi while only slightly suppressing the rise of cytosolic Ca^{2+} (Figures 6G, 6H, 6J, 6K, and S5). Next, we co-expressed GFP-OSBP and the SG marker NPY-mCherry in MIN6 cells and imaged them with total internal reflection fluorescence (TIRF) microscopy. Depolarization resulted in an enrichment of GFP-OSBP at SGs, which was counteracted by alkalization of the cytosol with NH_4Cl , indicating that Ca^{2+} increases facilitate the interaction between OSBP and SGs at least partly through acidification of the cytosol (Figures 6H–6K). Notably, we also found that acute addition of the OSBP inhibitor OSW-1 was associated with an acidification of the cytosol, seen as a drop in fluorescence intensity of cytosolically expressed pHluorin, implicating either roles of OSBP in pH regulation or off-target effects of the compound (Figure S5H).

Coordination of OSBP and Sac2 on the surface of SGs controls insulin secretion

Both SG PI(4)P and cholesterol are important for granule exocytosis. We and others recently showed that the PI(4)P phosphatase

Sac2 localized to SGs^{16,37} and that loss of Sac2 results in excess accumulation of PI(4)P on SGs. Insulin SGs are also a major storage site for cellular cholesterol,³⁸ shown here by the colocalization between the fluorescent cholesterol marker filipin and the SG markers NPY-GFP (Figure 7A) and insulin (Figures 7B and 7C). To explore the potential connection between SG cholesterol and PI(4)P, we first confirmed the localization of mCherry-Sac2 to SG (Figures 7D and 7E). Next, we performed siRNA-mediated knockdown of Sac2 in MIN6 cells and visualized cellular cholesterol using both fluorescently labeled cholesterol (Bodipy-cholesterol) and filipin. We found that Sac2 knockdown resulted in accumulation of cholesterol on intracellular structures, and that some, but not all of these structures colocalized with the SG marker NPY-mCherry (Figures S6B and S6C). Consistently, Sac2 knockdown caused a small but significant increase in filipin staining intensity on insulin-positive granules and there was also a trend toward an increased fraction of filipin-positive insulin granules in the Sac2-knockdown cells (Figures 7F and 7G). This indicates that SG PI(4)P may participate in cholesterol counter-transport. To test whether this transport depends on OSBP, we reduced OSBP expression by siRNA knockdown. OSBP knockdown caused a slight reduction in intracellular cholesterol, as determined by filipin staining, and, importantly, prevented the excess SG cholesterol accumulation induced by Sac2 knockdown (Figures 7H and 7I). These results indicate an interdependence of Sac2 and OSBP in controlling SG PI(4)P and cholesterol levels.

To test whether the Sac2- and OSBP-dependent changes in intracellular cholesterol had an impact on insulin secretion, we determined the effect of Sac2 or OSBP knockdown on depolarization-induced insulin secretion using an optical assay based on the detection VAMP2-pHluorin exocytosis by TIRF microscopy. Consistent with previous studies, both Sac2 KD and OSBP KD resulted in reduced insulin secretion (34% and 16%, respectively; Figures 7J and 7K).¹⁶ Simultaneous Sac2 and OSBP knockdown suppressed secretion to the same extent as OSBP knockdown alone (24%), and secretion was still significantly lower than under control conditions (Figures 7J and 7K). Similar results were obtained when glucose-stimulated insulin secretion was assessed using ELISA. siRNA-mediated knockdown of Sac2 reduced the secretory response to 55% of control, and simultaneous knockdown of OSBP did not restore the response

Figure 4. OSBP is recruited to insulin granules after OSW-1 treatment in live cells

(A) Confocal microscopy images of MIN6 cells expressing NPY-mNG and Halo^{JFX650}-OSBP, imaged live under basal conditions or following treatment with OSW-1 (20 nM for 20 min). Enlarged sections from the boxed regions are shown to the right. Scale bar: 10 μ m.
 (B) Means \pm SEM of OSBP-positive insulin granules from MIN6 cells expressing NPY-mNG and Halo^{JFX650}-OSBP following treatment with OSW-1 (20 nM for 20 min) or vehicle (DMSO). Each dot represents the average from one experiment (n = 11 replicates; Student's paired t test; ****p < 0.001).
 (C) TIRF microscopy images of MIN6 cells expressing NPY-mNG, RA-Sec61 β , and GB-OSBP, imaged live under basal conditions and following treatment with OSW-1 (20 nM for 20 min). Enlarged sections of the boxed regions are shown to the right. Scale bar: 10 μ m. Schematic of dimerization-dependent detection of ER-proximal OSBP in the absence or presence (yellow) of OSW-1 is shown to the right.
 (D) Manders coefficient of RA-Sec61 β /GB-OSBP signal overlapping with NPY-mNG puncta before and after treatment with 20 nM OSW-1 (means \pm SEM for n = 5 experiments; p < 0.05; Student's paired t test).
 (E) Confocal microscopy images of a MIN6 cell expressing RA-Sec61 β /GB-Rab3 and NPY-mNG under basal conditions (DMSO) and after 20-min treatment with 20 nM OSW-1. Scale bar: 10 μ m. Schematic of dimerization-dependent detection of ER-SG contacts in the absence or presence (yellow) of OSW-1 is shown to the right.
 (F) Manders coefficient of RA-Sec61 β /GB-Rab3 signal overlapping with NPY-mNG puncta before and after treatment with 20 nM OSW-1 (means \pm SEM for n = 33 cells from three experiments; non-significant; Student's paired t test).
 (G) Control or VAP-A/VAP-B double-knockdown INS-1 cells were treated with 50 nM OSW-1 (or vehicle) for 20 min, fixed, and immunostained against insulin and endogenous OSBP. After imaging with a point-scanning confocal microscope, Manders coefficients were quantified from three independent experiments. Each dot represents the mean of one experiment (*p < 0.05, **p < 0.01; two-tailed, unpaired Student's t test).

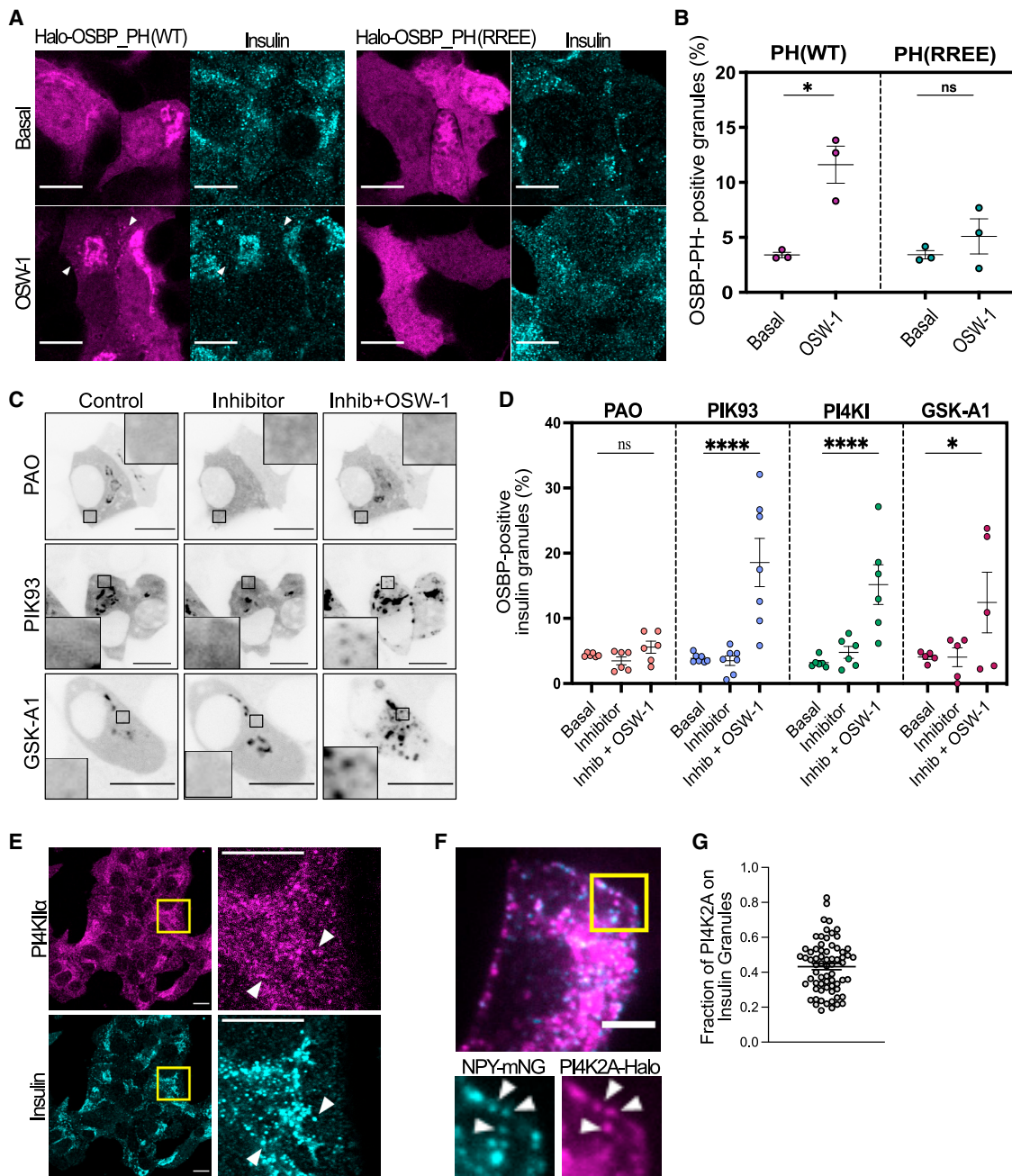


Figure 5. OSBP recognizes a granule-localized pool of PI(4)P

(A) Confocal microscopy images of MIN6 cells expressing Halo^{JFX650}-OSBP-PH or the non-PI4P-binding RR107/108EE mutant, treated with 50 nM OSW-1 (or vehicle) for 20 min, fixed, and immunostained against insulin. Scale bars: 5 μ m.

(B) Quantification of OSBP-PH-positive insulin granules from experiments done as in (A) (means \pm SEM, * p < 0.05; two-tailed unpaired Student's t test; n = 3).

(C) Confocal images of MIN6 cells expressing NPY-mNG (not shown) and Halo^{JFX650}-OSBP, treated with the indicated PI4-kinase inhibitors for 20 min followed by treatment with 20 nM OSW-1 for 20 min. Images have been inverted for clarity. Scale bar: 5 μ m.

(D) Quantifications of OSBP-positive granules from experiments performed as in (C). Each dot represents the average from one experiment (means \pm SEM; * p < 0.05, **** p < 0.0001; two-tailed paired Student's t test; n = 5–7 replicates).

(E) Confocal microscopy images of MIN6 cells immunostained against PI4K2A and insulin. Boxed region magnified to the right. Scale bar: 5 μ m.

(F) Confocal microscopy images and zoom-in of a MIN6 cell expressing the granule marker NPY-mNG and PI4K2A-Halo^{JFX650}. Scale bar: 5 μ m.

(G) Fraction of PI4K2A-Halo^{JFX650} fluorescence overlapping with NPY-mNG-positive granules (means \pm SEM; n = 68 cells).

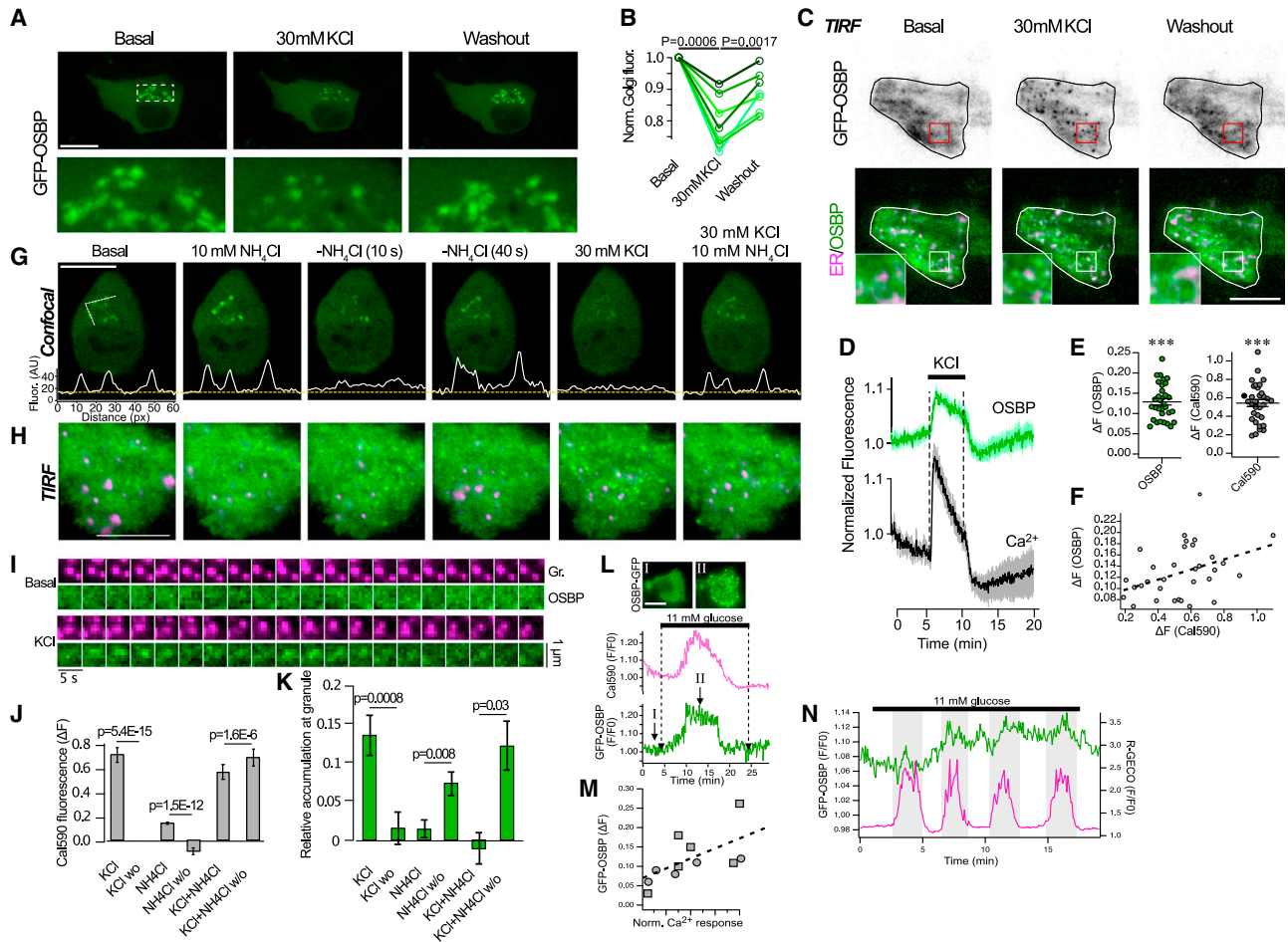


Figure 6. Spatial control of OSBP by Ca^{2+} and cytosolic pH

(A) Confocal microscopy images of a GFP-OSBP-expressing MIN6 cell following depolarization with 30 mM KCl. Images below are magnifications from the boxed area. Scale bar: 5 μm .

(B) Normalized Golgi GFP-OSBP fluorescence before, during, and after stimulation with 30 mM KCl ($n = 7$ cells; two-tailed paired Student's *t* test).

(C) TIRF microscopy images of a MIN6 cell expressing GFP-OSBP (black/green) and ER-mRFP (magenta) before, during, and after depolarization with 30 mM KCl. Note the appearance of GFP-OSBP puncta that overlap with the ER marker following depolarization.

(D) TIRF microscopy recordings from MIN6 cells expressing GFP-OSBP (green) and loaded with the Ca^{2+} indicator Cal590 (means \pm SEM for 32 cells from three experiments).

(E) Quantification of the plasma membrane fluorescence change in response to depolarization in MIN6 cells expressing GFP-OSBP and loaded with Cal590 (means \pm SEM; *** $p < 0.001$, Fisher's exact test; $n = 32$ cells from three experiments).

(F) Correlation between the depolarization-induced increase in Ca^{2+} and the appearance of GFP-OSBP at the plasma membrane.

(G) Confocal microscopy images of a MIN6 cell expressing GFP-OSBP and exposed to the indicated solutions. White line is an intensity profile plot across the Golgi.

(H) TIRF microscopy images of a MIN6 cells expressing GFP-OSBP (green) and NPY-mCherry (magenta) during stimulation with the indicated solutions.

(I) Time series from H showing the dynamic localization of GFP-OSBP to NPY-mCherry-positive granules (Gr.) following depolarization with 30 mM KCl.

(J) Quantification of Cal590 fluorescence change in response to the indicated stimulations (means \pm SEM; $n = 87$ cells; one-way ANOVA with Tukey's *post hoc* test).

(K) Quantifications of the relative accumulation of GFP-OSBP at NPY-mCherry-positive granules in response to the indicated stimulations (means \pm SEM; $n = 41$ cells; one-way ANOVA with Tukey's *post hoc* test).

(L) TIRF microscopy recording of GFP-OSBP (green) and Cal590 (magenta) fluorescence in response to 11 mM glucose. Images from before and during glucose stimulation are shown above.

(M) Correlation between the glucose-induced increase in Ca^{2+} and the appearance of GFP-OSBP at the plasma membrane ($n = 11$ cells).

(N) TIRF microscopy recording of GFP-OSBP and the Ca^{2+} indicator R-GECO fluorescence from a MIN6 cell during exposure to 11 mM glucose. Note that Ca^{2+} oscillations are mirrored by increases in GFP-OSBP at the plasma membrane.

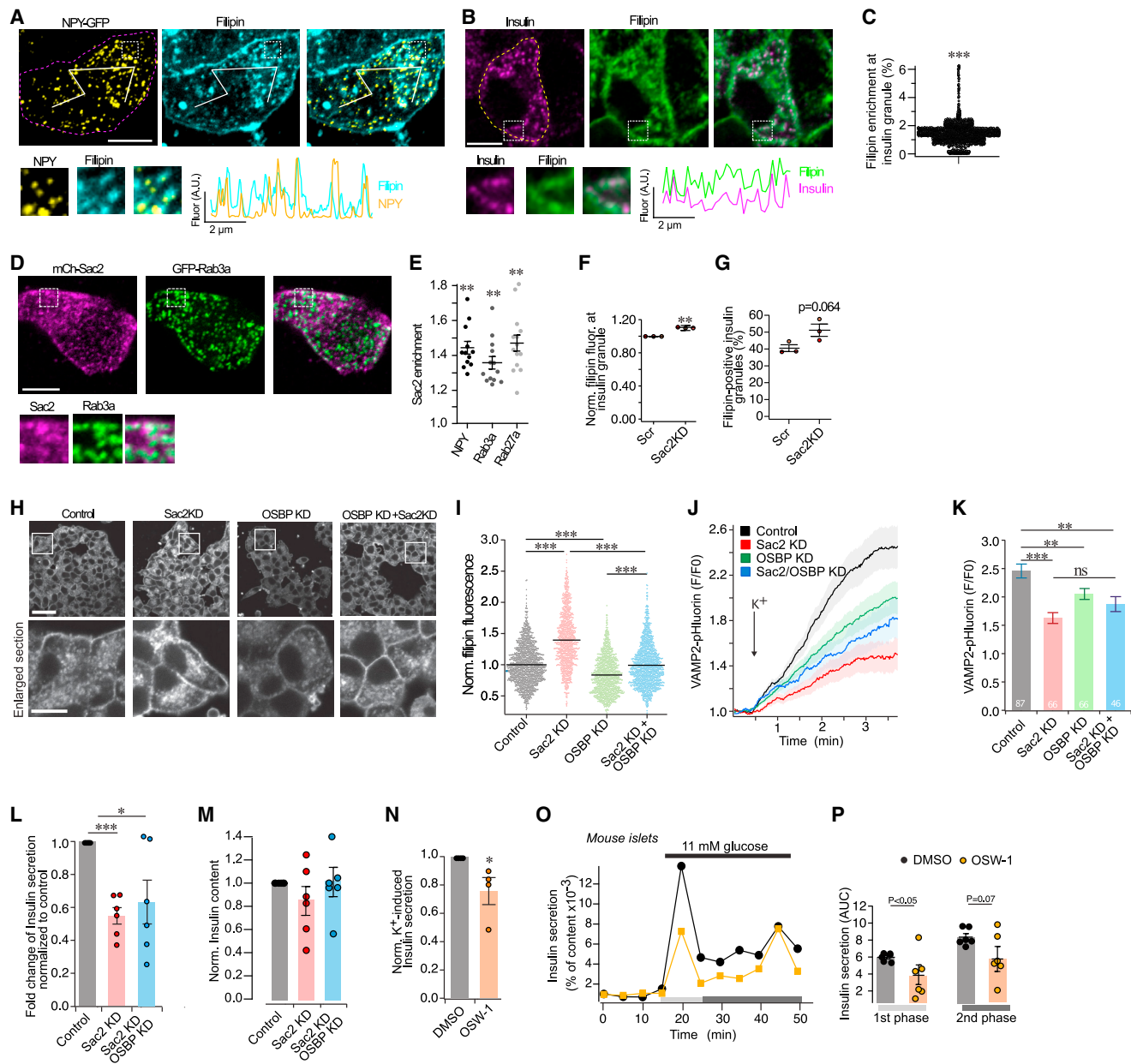


Figure 7. OSBP and Sac2 coordinately regulate insulin secretion

(A) Immunofluorescence image of MIN6 cells expressing NPY-GFP (yellow) and stained with filipin (cyan) to visualize cholesterol. An intensity profile from the white line is shown below. Scale bar: 5 μ m.

(B) Confocal microscopy images of a MIN6 cell immunostained for insulin (magenta) and stained with filipin (green). An intensity profile is shown below. Scale bar: 5 μ m.

(C) Enrichment of filipin on insulin-positive granules expressed as percentage above local background (** $p < 0.001$; two-tailed Student's *t* test).

(D) Confocal microscopy images of a MIN6 cells expressing the granule marker GFP-Rab3a (green) and mCherry-Sac2 (magenta). Scale bar: 5 μ m.

(E) Quantification of the relative enrichment of mCherry-Sac2 at insulin granules labeled with GFP-NPY, GFP-Rab3a, and GFP-Rab27 (means \pm SEM; $n = 12$ –14 cells; ** $p < 0.01$ for comparison to 1).

(F and G) Quantification of the relative enrichment of filipin on insulin granules (F) and of the fraction of insulin granules positive for filipin (G) in control and Sac2 knockdown MIN6 cells (means \pm SEM; $n = 3$ experiments; ** $p < 0.01$; two-tailed unpaired *t* test).

(H) Confocal microscopy images of filipin-stained MIN6 cells treated with control siRNA, siRNA against Sac2, OSBP, or Sac2 + OSBP. Scale bar: 40 μ m. Insets are magnifications of the boxed areas. Scale bar: 5 μ m.

(I) Normalized cytoplasmic filipin intensity in control MIN6 cells ($n = 1,604$) or MIN6 cells treated with siRNA against Sac2 ($n = 1,176$), OSBP ($n = 1,266$) or Sac2 + OSBP ($n = 1,492$) (means; *** $p < 0.0001$; ANOVA followed by Tukey's *post hoc* test).

(legend continued on next page)

to the level of control cells (Figure 7L). Insulin content was unaffected by both *Sac2* and *Sac2*/*OSBP* knockdown, indicating that the reduction in insulin secretion is due to impaired release and not production (Figure 7M). To more acutely test the involvement of *OSBP* in the regulation of insulin secretion, we incubated MIN6 cells with OSW-1 (20 nM) for 30 min and assessed the effect on depolarization-induced insulin secretion by ELISA. This time point was chosen because it is shorter than the time required for *de novo* synthesis of insulin SGs at the trans-Golgi network (TGN),²⁹ ruling out potential effects of OSW-1 treatment on SG biogenesis. We found that *OSBP* inhibition suppressed insulin secretion by 26% (Figure 7N) and that this effect was not due to inhibition of voltage-dependent Ca^{2+} influx (Figure S6). OSW-1 also inhibited glucose-stimulated insulin secretion from isolated mouse pancreatic islets without affecting Ca^{2+} influx (Figures 7O, 7P, and S6). These results show that lipid transport by *OSBP* is involved in the acute regulation of insulin secretion downstream of SG formation at the Golgi. The findings are consistent with a cooperative action between *Sac2* and *OSBP* on the surface of SGs of importance for normal insulin secretion.

DISCUSSION

In this study, we show that *OSBP* is recruited to SG through a Ca^{2+} - and pH-dependent process and that its stabilization at ER-SG contact sites depends on interactions between the N-terminal PH domain and SG PI(4)P and ER-localized VAPs. *OSBP* counter-transport PI(4)P for cholesterol at these contact sites, and both acute inhibition and siRNA-mediated knockdown of *OSBP*, as well as elevation of SG PI(4)P, resulted in impaired insulin secretion. Together, these results show the existence of physical contacts between the ER and SGs and demonstrate that these are sites of lipid transfer of importance for normal insulin secretion.

OSBP localization to ER-SG contact sites

The cholesterol concentration in the ER is only around 5 mol% of membrane lipids,³⁹ but it increases in the Golgi, at least in part through the action of *OSBP*. Mature insulin SGs are estimated to contain ~35 mol % cholesterol,^{38,40,41} comparable to concentrations found in the plasma membrane.³⁹ Given that a typical β cell contains around 10,000 SGs with a total surface area 4.5 times larger than the plasma membrane,² the granule pool of cholesterol represents a major storage site of the lipid in β cells.

It is generally assumed that the SG cholesterol is of Golgi origin, and Golgi-localized ABCG1 and ABCA1 have been shown to be important for SG cholesterol loading and for subsequent granule maturation.^{19,42,43} *OSBP* also contributes to SG cholesterol loading and biogenesis,¹⁹ but its localization in β cells has not been determined. We now show by live cell imaging and immunostainings of β cells and islets that *OSBP* primarily localizes to the TGN, but that it redistributes to a subset of insulin SGs after pharmacological inhibition with OSW-1, a condition that stabilizes the interaction between *OSBP* and target membranes.^{24,32} *OSBP* binding to SGs depended on interactions between the C-terminal PH domain and PI(4)P in the SG membrane and on interactions between the central FFAT motif and ER-localized VAP-A/B, similar to the canonical mechanism by which *OSBP* enriches at MCSs.^{23–25} These *OSBP*-positive MCSs form between the ER and mature, Rab3-positive SGs, although we cannot rule out the involvement of other granule populations since the methodology used for their detection was based on the presence of Rab3.

Role of ER-SG contacts in the regulation of insulin secretion

Directionality in *OSBP*-mediated lipid transport at the ER-Golgi interface is maintained by the action of the ER-localized PI(4)P phosphatase *Sac1* and Golgi-localized PI4-kinases.^{24,32} In accordance with this, we now find that SG-localized PI4-kinases promote *OSBP* binding, while the SG-localized PI(4)P phosphatase *Sac2* counteracts this process. Loss of *Sac2*, which we previously showed leads to accumulation of PI(4)P in the SG membrane,¹⁶ was accompanied by increased SG cholesterol content that was normalized by siRNA-mediated knockdown of *OSBP*. This shows that *OSBP* is involved in controlling SG PI(4)P and cholesterol levels at a point along the secretory pathway that is distal to budding from the TGN but precedes exocytosis at the plasma membrane. This provides the β cells with a mechanism to fine-tune the lipid content of SGs. Cholesterol is a critical component of the SG membrane, and both cholesterol excess and deficiency cause defects in insulin secretion.^{20,21,44,45} Our finding that inhibition of *OSBP* acutely suppresses insulin secretion is consistent with a role of *OSBP*-mediated PI(4)P/cholesterol exchange in the distal steps of the secretory pathway. This conclusion is also supported by the observation that insulin secretion, but not production, is suppressed in cells with reduced expression of *Sac2* or *OSBP*, findings that have also

(J) TIRF microscopy recordings of VAMP2-pHluorin fluorescence change in response to 30 mM K^+ in control cells and cells treated with siRNA against *Sac2*, *OSBP*, or *Sac2* + *OSBP*. Data presented as means \pm SEM for 47 (control), 31 (*sac2* KD), 42 (*OSBP* KD), and 21 (*Sac2* + *OSBP* KD) cells from one experiment.

(K) Means \pm SEM for the maximum VAMP2-pHluorin fluorescence increase in response to 30 mM K^+ in the indicated cells. Data from 87 (control), 66 (*Sac2* KD), 66 (*OSBP* KD), and 46 (*Sac2* + *OSBP* KD) cells from three experiments (** p < 0.01, *** p < 0.001; Kruskal-Wallis followed by Dunn's *post hoc* test).

(L) ELISA measurements of glucose-stimulated insulin secretion from MIN6 cells treated with control siRNA or siRNA against *Sac2* or *Sac2* + *OSBP*. Data are expressed as fold change in insulin secretion when the glucose concentration was increased from 3 to 20 mM and presented relative to control cells (means \pm SEM; n = 5; * p < 0.05, *** p < 0.001; Mann-Whitney U test).

(M) Insulin content in control cells or cells treated with control siRNA or siRNA against *Sac2* or *Sac2* + *OSBP* (means \pm SEM; n = 6).

(N) ELISA measurement of K^+ -induced insulin secretion in DMSO- (control) and OSW-1-treated (20 nM, 60 min) MIN6 cells (means \pm SEM; n = 4; * p < 0.05; Mann-Whitney U test).

(O) Insulin secretion from mouse islets perfused with the indicated glucose buffers. The islets were pre-treated for 30 min with DMSO (0.1 vol %; black) or OSW-1 (20 nM, orange).

(P) Quantification of the first- and second-phase insulin secretion from the perfused mouse islets in (K) (means \pm SEM; n = 5 for each condition; Mann-Whitney U test).

been reported in earlier studies.^{16,19} OSBP appears to be the only PI(4)P/cholesterol exchanger on SGs, as OSBP knockdown normalized cholesterol levels in SGs of Sac2-knockdown cells. However, despite having normal SG cholesterol, these cells still exhibited reduced insulin secretion, indicating that Sac2 regulates insulin secretion through additional mechanisms, potentially by regulating the activity of other lipid transport proteins that depend on PI(4)P.⁴⁶ ORP3 is an interesting candidate that counter-transport PI(4)P and phosphatidylcholine (PC),⁴⁷ a lipid that is present on SGs,⁴⁸ but whose function there is unknown.

Spatial control of OSBP

We found that the bulk of β cell OSBP localizes to the TGN under resting conditions, and clear localization to SGs was only seen after pharmacological inhibition. However, there must be physiological mechanisms that provide the cell control over OSBP distribution. It has been shown that Ca^{2+} can displace OSBP from the Golgi,^{33,34} and, consistent with such a mechanism, we now show that elevation of the cytosolic Ca^{2+} concentration, together with the ensuing acidification, resulted in displacement of OSBP from the Golgi that coincided with enhanced binding to SGs. How Ca^{2+} stabilizes OSBP at SGs and whether it is coupled to the displacement of OSBP from the Golgi or involves a cytosolic pool of OSBP is not clear. Inhibition of PI4-kinases also resulted in dissociation of OSBP from the Golgi but was not accompanied by accumulation on SGs, indicating either that PI4-kinase is required to maintain SG PI(4)P levels or that Ca^{2+} /pH promotes the association through additional mechanisms. Such mechanisms may involve pH-mediated changes in PI(4)P protonation,³⁵ direct effects of Ca^{2+} on OSBP³³ or PI(4)P,⁴⁹ as well as pH- or Ca^{2+} -induced clustering of PI(4)P in the target membrane.^{50,51} Irrespective of mechanism, the spatial control of OSBP by Ca^{2+} couples lipid exchange at the SG surface to Ca^{2+} -triggered exocytosis of SGs. Consistently, we find that acute inhibition of OSBP activity suppresses insulin secretion, indicating that OSBP acts immediately upstream of the exocytic process and distal to the formation of SGs at the Golgi. Further support for this notion comes from our observation that both ER-SG contacts and OSBP binding preferentially involve SGs located close to the plasma membrane. These physically docked granules are preferentially released in response to depolarization or during the first phase of glucose-stimulated insulin secretion, and both these mechanisms are also suppressed by OSBP inhibition. In addition to being physically docked at the plasma membrane, these SGs also represent a subpopulation of granules that has been recently formed at the TGN.⁹ It is therefore tempting to speculate that cholesterol transport at ER-SG contacts represents a key step in the maturation of newly formed SGs. Consistent with this notion, it has been shown that newly formed post-Golgi secretory vesicles are enriched for ergosterol and have a higher membrane order than the late Golgi membranes.⁵²

Concluding remarks

We propose a model where glucose-induced increases in Ca^{2+} , together with the ensuing acidification, facilitate interactions between OSBP and SGs. OSBP then participates in the controlled loading of cholesterol to the SG membrane in cooperation with the granule-localized PI(4)P phosphatase Sac2 in a process

that is required for normal insulin secretion. OSBP interacts with granules at ER-SG contact sites but does not seem to be involved in the formation of these contacts. Future research should aim at identifying protein complexes and biological processes that occur at these largely uncharacterized MCSs.

Limitations of the study

There are some limitations to this study that must be acknowledged. First, although we show in both live and fixed cells that OSBP localizes to ER-SG contacts in a manner similar to other MCSs, we do not provide direct evidence that it exchanges PI(4)P/cholesterol at this location. This would require the use of biosensors for detection of cholesterol, such as D4H,⁵³ as well as development of a biosensors that efficiently detects SG PI(4)P. Second, the pharmacological inhibitor of OSBP used in this study, OSW-1, has known off-target effects, e.g., NCX1,⁵⁴ which complicates interpretation of data. By using low concentrations and short incubation times, these off-target effects were likely minimized, yet the observation here that OSW-1 rapidly acidified the cytosol could potentially be explained by its effect on NCX1. Last, this work was performed solely on insulin-secreting β cells, and it remains to be shown whether the ER-SG contacts described here or the role of OSBP in SG maturation are general features of professional secretory cells.

STAR★METHODS

Detailed methods are provided in the online version of this paper and include the following:

- KEY RESOURCES TABLE
- RESOURCE AVAILABILITY
 - Lead contact
 - Materials availability
 - Data and code availability
- EXPERIMENTAL MODEL AND STUDY PARTICIPANT DETAILS
 - Cell culture
 - Pancreatic islet isolation and culture
- METHOD DETAILS
 - Reagents and plasmids
 - Transfection
 - Viral transduction of MIN6 cells
 - siRNA-mediated knockdown
 - Quantitative RT-PCR
 - Western blot
 - Immunofluorescence
 - Cholesterol visualization
 - Measurements of intracellular Ca^{2+} and pH
 - Insulin secretion measurements
 - OSW-1 treatment
 - Proximity ligation assay
 - Fluorescence microscopy
 - Electron microscopy
 - 3D segmentation of ER-insulin SG contact sites
 - Image analysis
- QUANTIFICATION AND STATISTICAL ANALYSIS

SUPPLEMENTAL INFORMATION

Supplemental information can be found online at <https://doi.org/10.1016/j.celrep.2024.113992>.

ACKNOWLEDGMENTS

We are grateful for the expert technical assistance provided by Dr. Beichen Xie, Ms. Cornelia Carleson, and Mrs. Antje Thonig. O.I.-H. was supported by grants from The Swedish Research Council (MH-2019-01456), The Novo Nordisk Foundation (NNF19OC0055275), Åke Wibergs stiftelse (M18-0146), Diabetesfonden (DIA2018-332), Magnus Bergwalls stiftelse (2018-02752), Familien Ernfors stiftelse, EFSD/Lilly, and EXODIAB. M.S. was supported with funds from the German Center for Diabetes Research (DZD e.V.); the German Ministry for Education and Research (BMBF); the Innovative Medicines Initiative 2 Joint Undertaking under grant agreement no. 115881 (RHAPSODY); and the Swiss State Secretariat for Education Research and Innovation (SERI; 16.0097-2). A.M. was the recipient of a MeDDrive grant from the Carl Gustav Carus Faculty of Medicine at TU Dresden. L.E. received support from The Swedish Research Council (2019-01406). A.T. received support from The Swedish Research Council (2021-02081), Swedish Diabetes Foundation, Diabetes Wellness Foundation, Family Ernfors Foundation, Nils Erik Holmsten's Foundation, Novo-Nordisk Foundation, and the Swedish national strategic grant initiative Excellence of Diabetes Research in Sweden (EXODIAB). A. Tomas was supported by UKRI Medical Research Council grants MR/R010676/1 and MR/X021467/1 as well as by UKRI COVID-19 Grant Extension Allocation (CoA), and further support from the EFSD, Diabetes UK, Eli Lilly, the Commonwealth, and the Integrated Biological Imaging Network (IBIN).

AUTHOR CONTRIBUTIONS

Conceptualization, S.P., K.W.T., P.M.N., O.I.-H.; methodology, S.P., K.W.T., and O.I.-H.; software, S.P. and A.M.; formal analysis, S.P., K.W.T., P.M.N., A.I.O., A. Tomas, and O.I.-H.; investigation, S.P., K.W.T., P.M.N., A.M., A.I.O., A.W., and O.I.-H.; resources, A.M., A. Tengholm, and M.S.; writing – original draft, O.I.-H. and P.M.N.; writing – review & editing, S.P., K.W.T., O.I.-H., A.M., L.E., and A.W.; visualization, S.P., K.W.T., P.M.N., and O.I.-H.; supervision, A. Tomas, L.E., A. Tengholm, M.S., and O.I.-H.; project administration, M.S. and O.I.-H.; funding acquisition, A. Tengholm, A. Tomas, L.E., M.S., and O.I.-H.

DECLARATION OF INTERESTS

The authors declare no competing interests.

Received: October 4, 2023

Revised: February 7, 2024

Accepted: March 7, 2024

Published: March 26, 2024

REFERENCES

- Omar-Hmeadi, M., and Idevall-Hagren, O. (2021). Insulin granule biogenesis and exocytosis. *Cell. Mol. Life Sci.* 78, 1957–1970. <https://doi.org/10.1007/s00018-020-03688-4>.
- Sato, T., and Herman, L. (1981). Stereological analysis of normal rabbit pancreatic islets. *Am. J. Anat.* 161, 71–84. <https://doi.org/10.1002/aja.1001610106>.
- Müller, A., Schmidt, D., Xu, C.S., Pang, S., D'Costa, J.V., Kretschmar, S., Münster, C., Kurth, T., Jug, F., Weigert, M., et al. (2021). 3D FIB-SEM reconstruction of microtubule-organelle interaction in whole primary mouse β cells. *J. Cell Biol.* 220, e202010039. <https://doi.org/10.1083/JCB.202010039>.
- Barg, S., Eliasson, L., Renström, E., and Rorsman, P. (2002). A subset of 50 secretory granules in close contact with L-type Ca^{2+} channels accounts for first-phase insulin secretion in mouse β -cells. *Diabetes* 51, S74–S82. <https://doi.org/10.2337/diabetes.51.2007.s74>.
- Olofsson, C.S., Göpel, S.O., Barg, S., Galvanovskis, J., Ma, X., Salehi, A., Rorsman, P., and Eliasson, L. (2002). Fast insulin secretion reflects exocytosis of docked granules in mouse pancreatic B-cells. *Pflügers Archiv* 444, 43–51. <https://doi.org/10.1007/s00424-002-0781-5>.
- Barg, S., Knowles, M.K., Chen, X., Midorikawa, M., and Almers, W. (2010). Syntaxin clusters assemble reversibly at sites of secretory granules in live cells. *Proc. Natl. Acad. Sci. USA* 107, 20804–20809. <https://doi.org/10.1073/pnas.1014823107>.
- Bracey, K.M., Ho, K.H., Yampolsky, D., Gu, G., Kaverina, I., and Holmes, W.R. (2020). Microtubules Regulate Localization and Availability of Insulin Granules in Pancreatic Beta Cells. *Biophys. J.* 118, 193–206. <https://doi.org/10.1016/j.bpj.2019.10.031>.
- Bokvist, K., Eliasson, L., Ammälä, C., Renström, E., and Rorsman, P. (1995). Co-localization of L-type Ca^{2+} channels and insulin-containing secretory granules and its significance for the initiation of exocytosis in mouse pancreatic B-cells. *EMBO J.* 14, 50–57. <https://doi.org/10.1002/j.1460-2075.1995.tb06974.x>.
- Ivanova, A., Kalaidzidis, Y., Dirx, R., Sarov, M., Gerlach, M., Schroth-Diez, B., Müller, A., Liu, Y., Andree, C., Mulligan, B., et al. (2013). Age-dependent labeling and imaging of insulin secretory granules. *Diabetes* 62, 3687–3696. <https://doi.org/10.2337/db12-1819>.
- Hoboth, P., Müller, A., Ivanova, A., Mziaut, H., Dehghany, J., Sönmez, A., Lachnit, M., Meyer-Hermann, M., Kalaidzidis, Y., and Solimena, M. (2015). Aged insulin granules display reduced microtubule-dependent mobility and are disposed within actin-positive microgranular bodies. *Proc. Natl. Acad. Sci. USA* 112, E667–E676. <https://doi.org/10.1073/pnas.1409542112>.
- Gandasi, N.R., Yin, P., Omar-Hmeadi, M., Ottosson Laakso, E., Vikman, P., and Barg, S. (2018). Glucose-Dependent Granule Docking Limits Insulin Secretion and Is Decreased in Human Type 2 Diabetes. *Cell Metabol.* 27, 470–478.e4. <https://doi.org/10.1016/j.cmet.2017.12.017>.
- Di Paolo, G., and De Camilli, P. (2006). Phosphoinositides in cell regulation and membrane dynamics. *Nature* 443, 651–657. <https://doi.org/10.1038/nature05185>.
- Cruz-Garcia, D., Ortega-Bellido, M., Scarpa, M., Villeneuve, J., Jovic, M., Porzner, M., Balla, T., Seufferlein, T., and Malhotra, V. (2013). Recruitment of arfapins to the trans-Golgi network by PI(4)P and their involvement in cargo export. *EMBO J.* 32, 1717–1729. <https://doi.org/10.1038/emboj.2013.116>.
- Dittié, A.S., Hajibagheri, N., and Tooze, S.A. (1996). The AP-1 adaptor complex binds to immature secretory granules from PC12 cells, and is regulated by ADP-ribosylation factor. *J. Cell Biol.* 132, 523–536. <https://doi.org/10.1083/jcb.132.4.523>.
- Olsen, H.L., Høy, M., Zhang, W., Bertorello, A.M., Bokvist, K., Capito, K., Efanov, A.M., Meister, B., Thams, P., Yang, S.N., et al. (2003). Phosphatidylinositol 4-kinase serves as a metabolic sensor and regulates priming of secretory granules in pancreatic β cells. *Proc. Natl. Acad. Sci. USA* 100, 5187–5192. <https://doi.org/10.1073/pnas.0931282100>.
- Nguyen, P.M., Gandasi, N.R., Xie, B., Sugahara, S., Xu, Y., and Idevall-Hagren, O. (2019). The PI(4)P phosphatase Sac2 controls insulin granule docking and release. *J. Cell Biol.* 218, 3714–3729. <https://doi.org/10.1083/jcb.201903121>.
- Ling, Y., Hayano, S., and Novick, P. (2014). Osh4p is needed to reduce the level of phosphatidylinositol-4-phosphate on secretory vesicles as they mature. *Mol. Biol. Cell* 25, 3389–3400. <https://doi.org/10.1091/mbc.E14-06-1087>.
- de Saint-Jean, M., Delfosse, V., Douguet, D., Chicanne, G., Payrastra, B., Bourguet, W., Antony, B., and Drin, G. (2011). Osh4p exchanges sterols for phosphatidylinositol 4-phosphate between lipid bilayers. *J. Cell Biol.* 195, 965–978. <https://doi.org/10.1083/jcb.201104062>.
- Hussain, S.S., Harris, M.T., Kreutzberger, A.J.B., Inouye, C.M., Doyle, C.A., Castle, A.M., Arvan, P., and Castle, J.D. (2018). Control of insulin

- granule formation and function by the ABC transporters ABCG1 and ABCA1 and by oxysterol binding protein OSBP. *Mol. Biol. Cell* 29, 1238–1257. <https://doi.org/10.1091/mbc.E17-08-0519>.
20. Hao, M., Head, W.S., Gunawardana, S.C., Hasty, A.H., and Piston, D.W. (2007). A Novel Mechanism for Pancreatic β -Cell Dysfunction, 56. <https://doi.org/10.2337/db07-0056.2-DG>.
 21. Xia, F., Xie, L., Mihic, A., Gao, X., Chen, Y., Gaisano, H.Y., and Tsushima, R.G. (2008). Inhibition of cholesterol biosynthesis impairs insulin secretion and voltage-gated calcium channel function in pancreatic β -cells. *Endocrinology* 149, 5136–5145. <https://doi.org/10.1210/en.2008-0161>.
 22. Xu, C.S., Pang, S., Shtengel, G., Müller, A., Ritter, A.T., Hoffman, H.K., Takemura, S.Y., Lu, Z., Pasolli, H.A., Iyer, N., et al. (2021). An open-access volume electron microscopy atlas of whole cells and tissues. *Nature* 599, 147–151. <https://doi.org/10.1038/s41586-021-03992-4>.
 23. Dong, R., Saheki, Y., Swarup, S., Lucast, L., Harper, J.W., and De Camilli, P. (2016). Endosome-ER Contacts Control Actin Nucleation and Retromer Function through VAP-Dependent Regulation of PI4P. *Cell* 166, 408–423. <https://doi.org/10.1016/j.cell.2016.06.037>.
 24. Mesmin, B., Bigay, J., Moser Von Filseck, J., Lacas-Gervais, S., Drin, G., and Antonny, B. (2013). XA four-step cycle driven by PI(4)P hydrolysis directs sterol/PI(4)P exchange by the ER-Golgi Tether OSBP. *Cell* 155, 830–843. <https://doi.org/10.1016/j.cell.2013.09.056>.
 25. Lim, C.Y., Davis, O.B., Shin, H.R., Zhang, J., Berdan, C.A., Jiang, X., Counihan, J.L., Ory, D.S., Nomura, D.K., and Zoncu, R. (2019). ER-lysosome contacts enable cholesterol sensing by mTORC1 and drive aberrant growth signalling in Niemann-Pick type C. *Nat. Cell Biol.* 21, 1206–1218. <https://doi.org/10.1038/s41556-019-0391-5>.
 26. Alford, S.C., Abdelfattah, A.S., Ding, Y., and Campbell, R.E. (2012). A fluorogenic red fluorescent protein heterodimer. *Chem. Biol.* 19, 353–360. <https://doi.org/10.1016/j.chembiol.2012.01.006>.
 27. Schauder, C.M., Wu, X., Saheki, Y., Narayanaswamy, P., Torta, F., Wenk, M.R., De Camilli, P., and Reinisch, K.M. (2014). Structure of a lipid-bound extended synaptotagmin indicates a role in lipid transfer. *Nature* 510, 552–555. <https://doi.org/10.1038/nature13269>.
 28. Gandasi, N.R., and Barg, S. (2014). Contact-induced clustering of syntaxin and munc18 docks secretory granules at the exocytosis site. *Nat. Commun.* 5, 3914. <https://doi.org/10.1038/ncomms4914>.
 29. Davidson, H.W., Rhodes, C.J., and Hutton, J.C. (1988). Intraorganellar calcium and pH control proinsulin cleavage in the pancreatic β cell via two distinct site-specific endopeptidases. *Nature* 333, 93–96. <https://doi.org/10.1038/333093a0>.
 30. Levine, T.P., and Munro, S. (2002). Targeting of Golgi-specific pleckstrin homology domains involves both PtdIns 4-kinase-dependent and -independent components. *Curr. Biol.* 12, 695–704. [https://doi.org/10.1016/S0960-9822\(02\)00779-0](https://doi.org/10.1016/S0960-9822(02)00779-0).
 31. Wyles, J.P., McMaster, C.R., and Ridgway, N.D. (2002). Vesicle-associated membrane protein-associated protein-A (VAP-A) interacts with the oxysterol-binding protein to modify export from the endoplasmic reticulum. *J. Biol. Chem.* 277, 29908–29918. <https://doi.org/10.1074/jbc.M201191200>.
 32. Mesmin, B., Bigay, J., Polidori, J., Jamecna, D., Lacas-Gervais, S., and Antonny, B. (2017). Sterol transfer, PI 4P consumption, and control of membrane lipid order by endogenous OSBP. *EMBO J.* 36, 3156–3174. <https://doi.org/10.15252/embj.201796687>.
 33. Malek, M., Wawrzyniak, A.M., Koch, P., Luchtenborg, C., Hessenberger, M., Sachsenheimer, T., Jang, W., Brügger, B., and Haucke, V. (2021). Inositol triphosphate-triggered calcium release blocks lipid exchange at endoplasmic reticulum-Golgi contact sites. *Nat. Commun.* 12, 2673. <https://doi.org/10.1038/s41467-021-22882-x>.
 34. Balla, A., Tuymetova, G., Tsiomenko, A., Várnai, P., and Balla, T. (2005). A Plasma Membrane Pool of Phosphatidylinositol 4-Phosphate Is Generated by Phosphatidylinositol 4-Kinase Type-III Alpha: Studies with the PH Domains of the Oxysterol Binding Protein and FAPP1. *Mol. Biol. Cell* 16, 1282–1295. <https://doi.org/10.1091/mbc.e04-07-0578>.
 35. Shin, J.J.H., Liu, P., Chan, L.J., Ullah, A., Pan, J., Borchers, C.H., Burke, J.E., Stefan, C., Smits, G.J., and Loewen, C.J.R. (2020). pH Biosensing by PI4P Regulates Cargo Sorting at the TGN. *Dev. Cell* 52, 461–476.e4. <https://doi.org/10.1016/j.devcel.2019.12.010>.
 36. Salgado, A., Silva, A.M., Santos, R.M., and Rosário, L.M. (1996). Multi-phasic action of glucose and α -ketoisocaproic acid on the cytosolic pH of pancreatic β -cells: Evidence for an acidification pathway linked to the stimulation of Ca²⁺ influx. *J. Biol. Chem.* 271, 8738–8746. <https://doi.org/10.1074/jbc.271.15.8738>.
 37. Cao, M., Park, D., Wu, Y., and De Camilli, P. (2020). Absence of Sac2/INPP5F enhances the phenotype of a Parkinson's disease mutation of synaptotagmin 1. *Proc. Natl. Acad. Sci. USA* 117, 12428–12434. <https://doi.org/10.1073/pnas.2004335117>.
 38. Galli, A., Arunagiri, A., Dule, N., Castagna, M., Marciani, P., and Perego, C. (2023). Cholesterol Redistribution in Pancreatic β -Cells: A Flexible Path to Regulate Insulin Secretion. *Biomolecules* 13, 224.
 39. Van Meer, G., Voelker, D.R., and Feigenson, G.W. (2008). Membrane Lipids: Where They Are and How They Behave. *Nat. Rev. Mol. Cell Biol.* 9, 112–124. <https://doi.org/10.1038/nrm2330>.
 40. Tsuchiya, M., Hosaka, M., Moriguchi, T., Zhang, S., Suda, M., Yokota-Hashimoto, H., Shinozuka, K., and Takeuchi, T. (2010). Cholesterol biosynthesis pathway intermediates and inhibitors regulate glucose-stimulated insulin secretion and secretory granule formation in pancreatic β -cells. *Endocrinology* 151, 4705–4716. <https://doi.org/10.1210/en.2010-0623>.
 41. Orci, L., Montesano, R., Meda, P., Malaisse-Lagae, F., Brown, D., Perrelet, A., and Vassalli, P. (1981). Heterogeneous distribution of filipin-cholesterol complexes across the cisternae of the Golgi apparatus. *Proc. Natl. Acad. Sci. USA* 78, 293–297. <https://doi.org/10.1073/pnas.78.1.293>.
 42. Kruit, J.K., Kremer, P.H.C., Dai, L., Tang, R., Ruddle, P., De Haan, W., Brunham, L.R., Verchere, C.B., and Hayden, M.R. (2010). Cholesterol efflux via ATP-binding cassette transporter A1 (ABCA1) and cholesterol uptake via the LDL receptor influences cholesterol-induced impairment of beta cell function in mice. *Diabetologia* 53, 1110–1119. <https://doi.org/10.1007/s00125-010-1691-2>.
 43. Harris, M.T., Hussain, S.S., Inouye, C.M., Castle, A.M., and Castle, J.D. (2018). Reinterpretation of the localization of the ATP binding cassette transporter ABCG1 in insulin-secreting cells and insights regarding its trafficking and function. *PLoS One* 13, 01983833–e198423. <https://doi.org/10.1371/journal.pone.0198383>.
 44. Bogan, J.S., Xu, Y., and Hao, M. (2012). Cholesterol Accumulation Increases Insulin Granule Size and Impairs Membrane Trafficking. *Traffic* 13, 1466–1480. <https://doi.org/10.1111/j.1600-0854.2012.01407.x>.
 45. Vikman, J., Jimenez-Feltström, J., Nyman, P., Thelin, J., and Eliasson, L. (2009). Insulin secretion is highly sensitive to desorption of plasma membrane cholesterol. *Faseb. J.* 23, 58–67. <https://doi.org/10.1096/fj.08-105734>.
 46. Nakatsu, F., and Kawasaki, A. (2021). Functions of Oxysterol-Binding Proteins at Membrane Contact Sites and Their Control by Phosphoinositide Metabolism. *Front. Cell Dev. Biol.* 9, 664788–664818. <https://doi.org/10.3389/fcell.2021.664788>.
 47. D'souza, R.S., Lim, J.Y., Turgut, A., Servage, K., Zhang, J., Orth, K., Sosale, N.G., Lazzara, M.J., Allegood, J., and Casanova, J.E. (2020). Calcium-stimulated disassembly of focal adhesions mediated by an orp3/iqsec1 complex. *Elife* 9, e54113–e54133. <https://doi.org/10.7554/eLife.54113>.
 48. MacDonald, M.J., Ade, L., Ntambi, J.M., Ansari, I.U.H., and Stoker, S.W. (2015). Characterization of phospholipids in insulin secretory granules and mitochondria in pancreatic beta cells and their changes with glucose stimulation. *J. Biol. Chem.* 290, 11075–11092. <https://doi.org/10.1074/jbc.M114.628420>.
 49. Kang, J.K., Kim, O.H., Hur, J., Yu, S.H., Lamichhane, S., Lee, J.W., Ojha, U., Hong, J.H., Lee, C.S., Cha, J.Y., et al. (2017). Increased intracellular Ca²⁺ concentrations prevent membrane localization of PH domains through the formation of Ca²⁺-phosphoinositides. *Proc. Natl. Acad. Sci. USA* 114, 11926–11931. <https://doi.org/10.1073/pnas.1706489114>.

50. Redfern, D.A., and Gericke, A. (2004). Domain Formation in Phosphatidylinositol Monophosphate/Phosphatidylcholine Mixed Vesicles. *Biophys. J.* *86*, 2980–2992. [https://doi.org/10.1016/S0006-3495\(04\)74348-9](https://doi.org/10.1016/S0006-3495(04)74348-9).
51. Sarmiento, M.J., Coutinho, A., Fedorov, A., Prieto, M., and Fernandes, F. (2014). Ca²⁺ induces PI(4,5)P₂ clusters on lipid bilayers at physiological PI(4,5)P₂ and Ca²⁺ concentrations. *Biochim. Biophys. Acta* *1838*, 822–830. <https://doi.org/10.1016/j.bbame.2013.11.020>.
52. Klemm, R.W., Ejsing, C.S., Surma, M.A., Kaiser, H.J., Gerl, M.J., Sampaio, J.L., De Robillard, Q., Ferguson, C., Proszynski, T.J., Shevchenko, A., and Simons, K. (2009). Segregation of sphingolipids and sterols during formation of secretory vesicles at the trans-Golgi network. *J. Cell Biol.* *185*, 601–612. <https://doi.org/10.1083/jcb.200901145>.
53. Maekawa, M., and Fairn, G.D. (2015). Complementary probes reveal that phosphatidylserine is required for the proper transbilayer distribution of cholesterol. *J. Cell Sci.* *128*, 1422–1433. <https://doi.org/10.1242/jcs.164715>.
54. Garcia-Prieto, C., Riaz Ahmed, K.B., Chen, Z., Zhou, Y., Hammoudi, N., Kang, Y., Lou, C., Mei, Y., Jin, Z., and Huang, P. (2013). Effective killing of leukemia cells by the natural product OSW-1 through disruption of cellular calcium homeostasis. *J. Biol. Chem.* *288*, 3240–3250. <https://doi.org/10.1074/jbc.M112.384776>.
55. Mazayaki, J., Araki, K., Yamato, E., Ikegami, H., Asano, T., Shibasaki, Y., Oka, Y., and Yamamura, K. (1990). Establishment of a pancreatic beta cell line that retains glucose-inducible insulin secretion: special reference to glucose transporter isoforms. *Endocrinology.* *127*, 126–132. <https://doi.org/10.1210/endo-127-1-126>.
56. Nakatsu, F., Messa, M., Nández, R., Czaplá, H., Zou, Y., Strittmatter, S.M., and de Camilli, P. (2015). Sac2/INPP5F is an inositol 4-phosphatase that functions in the endocytic pathway. *J. Cell Biol.* *209*, 85–95. <https://doi.org/10.1083/jcb.201409064>.
57. Gandasi, N.R., Vestö, K., Helou, M., Yin, P., Saras, J., and Barg, S. (2015). Survey of Red Fluorescence Proteins as Markers for Secretory Granule Exocytosis. *PLoS One* *10*, e0127801. <https://doi.org/10.1371/journal.pone.0127801>.
58. Idevall-Hagren, O., Dickson, E.J., Hille, B., Toomre, D.K., and De Camilli, P. (2012). Optogenetic control of phosphoinositide metabolism. *Proc. Natl. Acad. Sci. USA* *109*, E2316–E2323. <https://doi.org/10.1073/pnas.1211305109>.
59. Giordano, F., Saheki, Y., Idevall-Hagren, O., Colombo, S.F., Pirruccello, M., Milosevic, I., Gracheva, E.O., Bagriantsev, S.N., Borgese, N., and De Camilli, P. (2013). XPI(4,5)P₂-Dependent and Ca²⁺-Regulated ER-PM interactions mediated by the extended synaptotagmins. *Cell* *153*, 1494–1509. <https://doi.org/10.1016/j.cell.2013.05.026>.
60. Xie, B., Panagiotou, S., Cen, J., Gilon, P., Bergsten, P., and Idevall-Hagren, O. (2022). The endoplasmic reticulum–plasma membrane tethering protein TMEM24 is a regulator of cellular Ca²⁺ homeostasis. *J. Cell Sci.* *135*, jcs259073–14. <https://doi.org/10.1242/jcs.259073>.
61. Lee, J.E., Cathey, P.I., Wu, H., Parker, R., and Voeltz, G.K. (2020). Endoplasmic reticulum contact sites regulate the dynamics of membraneless organelles. *Science* *367*, eaay7108. <https://doi.org/10.1126/science.aay7108>.
62. Idevall-Hagren, O., Jakobsson, I., Xu, Y., and Tengholm, A. (2013). Spatial control of Epac2 activity by cAMP and Ca²⁺-mediated activation of ras in pancreatic β cells. *Sci. Signal.* *6*, ra29.1–S6. <https://doi.org/10.1126/scisignal.2003932>.

STAR★METHODS

KEY RESOURCES TABLE

REAGENT or RESOURCE	SOURCE	IDENTIFIER
Antibodies		
Calnexin	Invitrogen	Cat# PA5-34754; RRID: AB_2552106
Chromogranin A	Proteintech	Cat# 10529-1-AP; RRID: AB_2081122
GolgiB1	Bioss	Cat# BS-13356R
Insulin	Dako	Cat# A0564; RRID: AB_10013624
IP3R1	Abcam	Cat# ab264281
OSBP	Invitrogen	Cat# PA5-30110; RRID: AB_2547584
PI4K2A	Santa Cruz Biotechnology	Cat# sc-390026
Rab3	Synaptic Systems	Cat# 107 111
VAPA	Atlas Antibodies	Cat# HPA009174; RRID: AB_1080549
VAPB	Atlas Antibodies	Cat# HPA013144; RRID: AB_1858717
b-actin	Santa Cruz Biotechnology	Cat# sc-47778; RRID: AB_626632
Bacterial and virus strains		
Ad-CMV-GB-Rab3	Vector Biolabs	Lot# 20220125T#2
Ad-CMV-RA-Sec61b	Vector Biolabs	Lot# 20220125T#3
Chemicals, peptides, and recombinant proteins		
BCECF	Life technologies	Cat# B1170
Cal-520-AM	AAT Bioquest	Cat# 21130
Cal-590-AM	AAT Bioquest	Cat# 20510
OSW-1	Cayman Chemical	Cat# 30310
TopFluor Cholesterol (23-[dipyrometheneboron difluoride]-24-norcholesterol]	Avanti Polar Lipids, Inc.	Cat# 810255
Filipin III	Cayman Chemical	Cat# 70440
JFX650 Halotag Ligand	Lavis Lab (Janalia Research Campus)	N/A
JF549 Halotag Ligand	Lavis Lab (Janalia Research Campus)	N/A
JFX646 Halotag Ligand	Lavis Lab (Janalia Research Campus)	N/A
Carbamoyl chloride	Tocris	Cat# 2810
Phenylarsine oxide	Sigma Aldrich	Cat# P3075
PIK 93	Sigma Aldrich	Cat# SML0546
PI4KI	MedChemExpress	Cat# HW-100198
GSK-A1	Sigma Aldrich	Cat# SML2453
Critical commercial assays		
Cholesterol Assay Kit	Abcam	Cat# Ab122116
Lipofectamine™ 2000	Life Technologies	Cat# 11668019
Lipofectamine™ 3000	Life Technologies	Cat# L3000015
Lipofectamine™ RNAiMAX	Life Technologies	Cat# 13778150
NaveniFlex 100 MR	Navinci	NC.MR.100 Red
QuantiTect SYBR Green RT-PCR kit	Qiagen	Cat# 204443
Deposited Data		
FIB-SEM dataset of a mouse pancreas	OpenOrganelle	https://open.quiltdata.com/b/janelia-cosem-datasets/tree/jrc_mus-pancreas-3/jrc_mus-pancreas-3.n5/em/
Experimental models: Cell lines		
MIN6 cells	Yamamura Lab	Mazayaki et al. ⁵⁵
Ins-1 cells	Alejandra Tomas (Imperial College, UK)	N/A

(Continued on next page)

Continued

REAGENT or RESOURCE	SOURCE	IDENTIFIER
Experimental models: Organisms/strains		
C57Bl6J mice	Scanbur	N/A
Oligonucleotides		
PCR Primers	Eurofins (See Table S1 in Supplementary figures)	N/A
Recombinant DNA		
pLJM1-FLAG-GFP-OSBP	Addgene	Plasmid #134659
GFP-Sac2	Pietro De Camilli lab	Nakatsu et al. ⁵⁶
VAPA-GFP	Pietro De Camilli lab	Dong et al. ²³
VAMP2-pHluorin	Idevall-Hagren lab	Nguyen et al. ¹⁶
RA-Sec61 β	Addgene	Plasmid #153978
GB-Dcp1	Addgene	Plasmid #153979
NPY-mNG	This paper	N/A
PI4K2A-Halo	This paper	N/A
NPY-mCherry	Barg lab	Gandasi et al. ⁵⁷
NPY-GFP	Barg Lab	Gandasi et al. ⁵⁷
Software and algorithms		
Cell Profiler	open-source	N/A
MetaFluor	Molecular Devices	N/A
MetaMorph	Molecular Devices	N/A
Prism9	GraphPad Software	N/A
ImageJ	Fiji	N/A

RESOURCE AVAILABILITY

Lead contact

Further information and requests for resources and reagents should be directed to and will be fulfilled by the lead contact, Olof Idevall-Hagren (olof.idevall@mcb.uu.se).

Materials availability

All unique/stable reagents generated in this study are available from the [lead contact](#) without restriction.

Data and code availability

- All data reported in this paper will be shared by the [lead contact](#) upon request.
- This paper does not report original code.
- Any additional information required to reanalyze the data reported in this work paper is available from the [lead contact](#) upon request.

EXPERIMENTAL MODEL AND STUDY PARTICIPANT DETAILS

Cell culture

MIN6 cells were used between passages 18 to 35 and kept in cell culture medium composed of DMEM supplemented with 4.5 g/L glucose, 2mM L-glutamine, 100U/mL Penicillin, 100 μ g/mL Streptomycin, 50 μ M 2-mercaptoethanol, and 15% fetal bovine serum (all from Life Technologies). INS-1 832/3 cells were cultured in RPMI-1640 supplemented with 11 mM glucose, 2mM L-glutamine, 100 μ g/mL Streptomycin, 100U/mL Penicillin and 10% fetal bovine serum. All cells were cultured in a humidified atmosphere at 37°C and 5% CO₂.

Pancreatic islet isolation and culture

All animal experimental procedures were approved by the local ethics committee for use of laboratory animals in Uppsala, Sweden. Islets of Langerhans were isolated from 4 to 12-month-old C57Bl6J mice by collagenase digestion of the pancreas followed by hand-picking of individual islets. After isolation, the islets were cultured for 1–3 days in RPMI 1640 medium containing 5.5 mM glucose, 10% fetal calf serum, 100 U/mL penicillin and 100 μ g/mL streptomycin at 37°C in a 5% CO₂ humidified atmosphere. 20–50 freshly isolated islets were infected with 10 μ L of high titration virus in 100 μ L of culture medium (RA-Sec61b; 5.5 \times 10¹⁰ PFU/mL, GB-Rab3; 4.5 \times 10¹⁰

PFU/mL; Vector Biolabs, Malvern, PA). After 3 h, the coverslips were washed with medium and the cells were cultured for at least two days to allow the expression of the contact sites reporter before performing experiments. Human islets were isolated from the pancreas of cadaveric organ donors by the Nordic Network for Clinical Islet Transplantation Uppsala (ethical approval by Uppsala Regional Ethics Board) with written donor and family consent for use in research. Work with human tissue complied with all relevant ethical regulations for use of human tissue in research and the study was approved by the Uppsala Regional Ethics Board (2006/348). Isolated islets were cultured free-floating in sterile dishes in CMRL 1066 culture medium containing 5.5 mM glucose, 10% fetal calf serum (FCS), 2 mM L-glutamine, streptomycin (100 U/ml), and penicillin (100 U/ml) at 37 °C in an atmosphere of 5% CO₂ for up to 2 weeks.

METHOD DETAILS

Reagents and plasmids

TopFluor Cholesterol (23-[dipyrrometheneboron difluoride]-24-norcholesterol) was from Avanti Polar Lipids, Inc. Cholesterol Assay Kit (Cell-Based) was from Abcam (Ab122116). OSW-1 was from Cayman Chemical. Cal-590-AM and Cal520-AM were from AAT Bioquest. BCECF was from Life technologies. Plasmids pLJM1-FLAG-GFP-OSBP was from Addgene (Plasmid #134659,²⁵ GFP-Sac2 and VAPA-GFP were gifts from Pietro De Camilli,^{23,56} GFP-Rab3a, NPY-mCherry, NPY-mNG and VAMP2-pHluorin were gifts from Sebastian Barg, Uppsala University, Sweden. RA-Sec61β and GB-Dcp1 were gifts from Gia Voeltz (Addgene plasmid #153978, #153979). Halo-OSBP was created by amplifying OSBP from pLJM1-FLAG-GFP-OSBP (Addgene #134659) and inserting it by Gibson Assembly (New England Biolabs) into the BglII/NotI sites of a customized cloning vector bearing an N-terminal Halo-tag (pENTR20-Halo-C1). This vector was recombined using Gateway LR reaction (Invitrogen) into a customized Gateway-enabled pCDH vector (System Biosciences) and expressed under control of a EF1α promoter. GB-Rab3 was created by amplifying mouse Rab3a ORF and inserting it into the XhoI/SacII site of the GB-Dcp1 using the following primers: FW: 5'-GATCTCGAGTACCGGTTG GATCAGGATCAATGGCCTCAGCCACAGAC-3'

RV: 5'-GGGCCCGCGTCCAGCAGGCGCAATCC-3'. GB-OSBP was generated by amplifying OSBP from Halo-OSBP using the following primers: FW: 5'-CAAGTCCGGACTCAGATCCATGGCTGCTACGGAGC-3', RV: 5'-CAGTTATCTAGATCCGGTGGATCTCA GAAAATGTCCGGGCATG-3' followed by ligation to pGB-Dcp1 using XhoI/XmaI. GB-CAAX was generated by releasing Rab3 from GB-Rab3 with NheI/AgeI followed by ligation to pCIBN-CAAX.⁵⁸ RA-CAAX was generated by releasing RA from RA-Sec61β with NheI/AgeI followed by ligation to pGB-CAAX. GB-E-Syt3 was generated by releasing E-Syt3 from pEGFP-E-Syt3⁵⁹ with NheI/XhoI followed by ligation to pGB-Dcp1. E-Syt3-GB was generated by releasing E-Syt3 from pE-Syt3-EGFP with NheI/AgeI followed by ligation to pTOM20-GB.⁶⁰ RA-Rab3 was generated by releasing Rab3 from GB-Rab3 with XhoI/SacII followed by ligation to pRA-Sec61β.⁶¹ GB-Sec61β was generated by releasing GB from pGB-Dcp1⁶¹ with NheI/XhoI followed by ligation to pRA-Sec61β. Adenoviral particles (E5 serotype) carrying RA-Sec61β and GB-Rab3a under the control of CMV-promoters were produced by Vector Biolabs (Malvern, PA). The following antibodies were used in the study: OSBP Polyclonal (catalog no. PA5-30110, host: rabbit, 1:300, Invitrogen), VAPA polyclonal (HPA009174, Atlas Antibodies, host: Rabbit, 1:400), VAPB polyclonal (HPA013144, Atlas Antibodies, host: Rabbit, 1:400), PI4K2A monoclonal (sc-390026, Santa Cruz, host: mouse, 1:100), β-actin monoclonal (clone C4, sc-47778, Santa Cruz Biotechnology, host: mouse, 1:300), IP3R1 polyclonal (catalog no. ab264281, Abcam, host: rabbit, 1:500), Rab3 monoclonal (catalog no. 107 111, Synaptic Systems, host: mouse, 1:500), Chromogranin A polyclonal (catalog no. 10529-1-AP, Proteintech, host: Rabbit, 1:400), insulin polyclonal (catalog no. A0564, Dako, host: guinea pig, 1:1000), calnexin (PA5-34754, Invitrogen, host: Rabbit, 1:500), GolgB1 (BS-13356R, Bioss, host: rabbit, 1:500).

Transfection

Reverse transfections were carried out in 100 μL of OptiMEM with 0.5 μL Lipofectamine 2000 or Lipofectamine 3000 (all from Life Technologies), 0.1–0.4 μg plasmid DNA, and 200,000 cells. The transfection was terminated after 3–5 h, and imaging was done between 22 and 30 h after transfection.

Viral transduction of MIN6 cells

MIN6 cells were infected with 10 μL of high titration virus in 100 μL of culture medium (RA-Sec61b; 5.5 × 10¹⁰ PFU/mL, GB-Rab3; 4.5 × 10¹⁰ PFU/mL; Vector Biolabs, Malvern, PA). After 3 h, the coverslips were washed with medium and the cells were cultured for at least two days to allow the expression of the contact sites reporter before performing experiments.

siRNA-mediated knockdown

Sac2 knockdown was performed with siRNA targeting mouse gene sequence Inpp5f: 5'-GGAAUGCGGUAAACGAATT-3' and was from Ambion (Life Technologies). OSBP knockdown was performed using ON-TARGET plus SMART pool Mouse OSBP siRNA from Dharmacon. MIN6 cells were transfected in 12 well-plates with siRNA using Lipofectamine 2000, followed by a second round of transfection 3–4 h later using RNAiMax (Life Technologies) according to the manufacturer's instructions with final siRNA concentration of 50 nM and 20 nM for Sac2 and OSBP, respectively. ON-TARGET plus NON-targeting Pool from Dharmacon was used as control.

INS-1 832/3 cells were transfected with 40 nM of Control (Ambion Silencer Select Negative Control #1 siRNA; Cat no: 4390843) or VAPA+B siRNA (Ambion Silencer Select Pre-Designed siRNAs; Cat#:4390771), using Lipofectamine 2000 according to the manufacturer's instructions, and transferred to glass coverslips the next day.

Quantitative RT-PCR

Sac2 knockdown was confirmed by quantitative RT-PCR using QuantiTect SYBR Green RT-PCR kit (Qiagen) and the following primers: Sac2-fwd: 5'TAAGGAGAGCCAGAGAAGCCA-3', Sac2-rev: 5-CAGCAGCACTTCCACATCTCT-3'; GAPDH-fwd: 5'-ACTC CACTCACGGCAAATTC-3'; GAPDH-rev: 5'-TCTCCATGGTGGTGAAGACA-3'. PCR reactions were performed using Light Cycler 2.0 (Roche). Results are expressed as $\Delta\Delta C_t$, normalized to the expression in control samples.

Western blot

Cells were lysed on ice with RIPA buffer (50 mM Tris-HCl, pH 7.4, 1% NP-40, 0.5% Na-deoxycholate, 0.1% SDS, and 10% EDTA) supplemented with a protease inhibitor cocktail (Roche). Samples were cleared by centrifugation and protein concentration was measured by the Bradford assay. OSBP knockdown was confirmed by Western blotting using OSBP Polyclonal Antibody (1:1000, Invitrogen) and β -actin mouse monoclonal (clone C4, sc-47778, 1:300, Santa Cruz Biotechnology).

Immunofluorescence

Cells grown on monolayers were fixed in 4% paraformaldehyde in either PBS or PHEM buffer (60mM PIPES, 25mM HEPES, 10mM EGTA, 4mM MgSO₄, pH 6.9) for 20 min at RT, followed by 3 washes of buffer. Permeabilization was performed using 0.1–0.2% Triton X-100 for 10–15mins, followed by 3 washes of buffer, and followed by blocking for 1hr in buffer containing 2% BSA. Primary antibody incubation was carried out overnight at 4°C in blocking buffer, washed 3 times and incubated for 1hr with secondary antibody in blocking buffer. Coverslips were then washed 3 times, mounted in Prolong Glass (Invitrogen) and left to dry for at least 18hr before imaging. Where NPY-mNeonGreen was visualized in fixed samples, the secondary antibody incubation included 5nM of Fluotag-X2-anti-mNeonGreen conjugated to Atto488 (Nanotag Biotechnologies).

Cholesterol visualization

TopFluor cholesterol was diluted (0.6 mg/mL) in methanol:water (95:5 vol%) followed by sonication. The dissolved cholesterol was transferred to glass tubes and dried under N₂, followed by resuspension in 4 mg/mL fatty acid free BSA. MIN6 cells were loaded with 1 μ M TopFluor cholesterol and incubated for 3 h followed by additional culture in a cholesterol-free medium for 15–18 h prior live cell imaging. Filipin cholesterol staining was performed following the manufacturer's instructions (Ab122116 - Cholesterol Assay Kit, Abcam) and imaging was performed 0–4 h after staining.

Measurements of intracellular Ca²⁺ and pH

To measure changes in the intracellular Ca²⁺ concentrations, MIN6 cells or mouse islets were preincubated at 37°C for 30 min in an experimental buffer (see below) supplemented with 2 μ M of the AM-ester-form of the Ca²⁺-indicator Cal-520. The cells were subsequently washed twice with experimental buffer before visualization by fluorescence microscopy (excitation 491 nm, emission 530/50 nm). Intracellular pH was determined using the ratiometric dye BCECF. MIN6 cells were incubated with 2 μ M of the AM-ester-form of BCECF for 30 min at 37°C, followed by two washing steps to remove residual indicator and visualization by fluorescence microscopy (excitation 442 nm and 491 nm, emission 530/50 nm).

Insulin secretion measurements

MIN6 cells were cultured in 12-well plates to approximately 70% confluency. Cells were washed three times with PBS, pre-incubated in experimental buffer (125mM NaCl, 4.9mM KCl, 1.2mM MgCl₂, 1.3mM CaCl₂, 25mM HEPESHepes, and 0.1% BSA) with 3mM Glucose for 30 min at 37°C. Cells were then incubated for 30 min in experimental buffer with 3mM glucose, 20mM glucose or 3mM glucose and 30 mM KCl. The supernatants were collected for insulin measurement using a Mouse Insulin ELISA kit (Mercodia, Uppsala, Sweden). Isolated mouse islets of Langerhans (8–10 islets per experiment) were placed in a closed 10 μ L chamber made of Teflon tubing with a fine mesh plastic net at the outlet that prevented the islets from escaping. Islets were subsequently perfused with experimental buffer. The perfusate was collected in 5 min fractions and insulin content in the fractions was determined using a mouse insulin ELISA kit (Mercodia). Cells were subsequently collected, diluted in acidic ethanol (75% EtOH and 15% HCl) and sonicated for 2 \times 10 s to determine the insulin content.

OSW-1 treatment

Cells were incubated in experimental buffer containing either 0.1% DMSO or 20nM OSW-1 (dissolved in DMSO) for 30 min at 37°C before imaging or ELISA sample collection.

Proximity ligation assay

PLA was performed according to the manufacturer's recommendation (Navinci NaveniFlex MR). Primary antibodies against VAP-A (HPA009174, rabbit polyclonal, Sigma Aldrich), SEC61 (ab15576, rabbit polyclonal, Abcam) and Rab3 (catalog no. 107 111, mouse monoclonal, Synaptic Systems) were used at 1:200 dilution.

Fluorescence microscopy

All experiments, unless otherwise stated, were performed at 37°C in an experimental buffer containing 125 mM NaCl, 4.9 mM KCl, 1.2 mM MgCl₂, 1.3 mM CaCl₂, 25 mM HEPESHepes, 3 mM D-Glucose, and 0.1% BSA (pH 7.40). Cells were preincubated in imaging

buffer for 30 min before experiments, and continuously perfused with the same buffer at the stage of the microscope. Where required, Halo-tagged proteins were labeled with 40nM of Halo-tag ligand bearing JFX646 (Grimm et al., 2021) for 20 min in experimental buffer and unbound ligand was washed out for 10 min in the same buffer. Confocal microscopy was performed on a Nikon Eclipse Ti-2 equipped with a Yokogawa CSU-10 spinning disc confocal unit and a 100×/1.49-NA plan Apochromat objective (Nikon) as previously described.⁶² Briefly, excitation light was provided by 491-nm, 561-nm DPSS lasers and 640-nm diode laser (all from Cobolt), and fluorescence was detected through interference filters 530/50-nm (GFP, mNG, Alexa 488), 590/20-nm (mCherry, RA, Alexa 568) or 650LP filter (JF646) with a back-illuminated EMCCD camera (DU-888; Andor Technology) controlled by MetaFluor software (Molecular Devices). TIRF microscopy was performed on two different setups. A custom-built prism-type TIRF microscope equipped a 16×/0.8-NA water-immersion objective (Nikon) was used for low-magnification imaging of cell populations as previously described.⁶² It is built around an E600FN upright microscope (Nikon) contained in an acrylic glass box thermostated at 37°C by an air stream incubator. DPSS lasers (Cobolt) provided 491-nm and 561-nm light for excitation of GFP and mCherry. The laser beams were merged with dichroic mirrors (Chroma Technology), homogenized, and expanded by a rotating Light Shaping Diffuser (Physical Optics) before being refocused through a modified quartz dove prism (Axicon) with a 70° angle to achieve total internal reflection. Laser lines were selected with interference filters (Semrock) in a motorized filter wheel equipped with a shutter (Sutter Instruments) blocking the beam between image captures. Fluorescence from the cells was detected at 530/50 nm for GFP (Semrock interference filters) or 597LP for mCherry (Melles Griot glass filter) with an EM-CCD camera (Andor DU-887) under MetaFluor software control. TIRF imaging was also performed on an inverted Nikon Ti-E equipped with a TIRF illuminator and a 60×1.45-NA objective (all Nikon). Excitation light was provided by diode-pumped solid-state lasers (491-nm, 561-nm) or diode lasers (640-nm; all from Cobolt). Lasers were merged with dichroic mirrors (Chroma technologies) and excitation light was selected with bandpass filters mounted in a filter wheel (Sutter Instruments Lambda 10-3) and delivered to a fiber optic cable and delivered to the TIRF illuminator. Excitation light was reflected through the objective with a dichroic mirror (ZET405/488/561/640m-TRFv2, Chroma Technologies) and emission light was separated using interference (530/50 nm, 590/20-nm) or long pass (650LP) filters (Semrock) mounted in a filter wheel (Sutter Instruments Lambda 10-3). An electronic shutter was used to block light exposure between image captures. Emission light was detected using an Orca-AR camera controlled by MetaFluor software (Molecular Devices Corp.). Filipin imaging was visualized on a laser scanning confocal microscope (Zeiss LSM 780) equipped with a Plan-Apo 20X/0.8-NA objective using a 405-nm diode laser.

For INS-1 cells, confocal images were captured with a Zeiss LSM-780 inverted microscope from the Facility for Imaging by Light Microscopy at Imperial College London using a 63x/1.40 Oil DIC Plan-Apochromat objective and analyzed using colocal-2 plugin in Fiji.

Electron microscopy

Mouse or human islets were hand-picked under a microscope and groups of ~50 isolated islets were fixed in Millonig's buffer with 2.5% glutaraldehyde overnight, post-fixed in 1.0% osmium tetroxide, dehydrated and embedded in AGAR 100 (Oxfors Instruments Nordiska AB, Sweden). Before visualization 70–90 nm sections were cut, mounted, and contrasted. The samples were examined in a JEM 1230 electron microscope (JEOL-USA, Inc, MA, USA).

3D segmentation of ER-insulin SG contact sites

Segmentation of ER-SG contact sites was performed on focused ion beam electron microscopy (FIB-SEM) volumes of isolated mouse pancreatic islets previously acquired for and available via the openorganelle platform (<https://openorganelle.janelia.org/>) under a CC BY 4.0 license (Xu et al., 2021). Small volumes with contact sites were cut in FIJI (Schindelin et al., 2012) and manual segmentation of ER and SG was performed with the Labkit FIJI plugin (Arzt et al., 2022). Ribosomes were segmented by black-and-white-thresholding in Microscopy Image Browser (Belevich et al., 2016). Segmentation results were rendered with ORS Dragonfly (<https://www.theobjects.com/dragonfly/index.html>).

Image analysis

TIRF microscopy images were analyzed offline using ImageJ. Briefly, for analysis of VAMP2-pHluorin and Cal-520 experiments, cell footprints were manually identified and regions of interest covering the edges of the adherent cells were drawn. Intensity changes within these regions during the experiments were measured and exported to Excel. All data points were background corrected, followed by normalization to the pre-stimulatory level (F/F₀). Analysis of enrichment of tagged proteins to insulin SGs was performed using a pipeline assembled in Cell Profiler. Insulin SGs were segmented using the NPY channel. Cells positive for the protein of interest were segmented and all insulin SGs not in an OSBP-positive cell were discarded. The median fluorescence in a 2-pixel wide ring around each insulin SG was defined as the background and the enrichment of the protein of interest was calculated by dividing the mean of fluorescence in each insulin granule with its corresponding background. To determine the percentage of insulin SG positive for a protein, we set the enrichment threshold at 2 standard deviations from the mean. For each treatment, the standard deviations for the basal condition were computed and used for their corresponding treatment conditions.

QUANTIFICATION AND STATISTICAL ANALYSIS

Statistical analysis was performed using two-way ANOVA followed by Tukey's post hoc test or Kruskal-Wallis followed by Dunn's (for non-parametric data) post hoc tests. Where a single test group was compared against a treatment group, we performed Student's

2-tailed unpaired t test or Mann-Whitney U-test (for non-parametric data). Paired analysis was performed with Student's 2-tailed paired t test. We did not perform a power analysis and the experiments did not have a predetermined sample size, but this was instead chosen based on experience. At least three independent experiments (performed on separate days) were used for all analyses.